ANSWERS TO REFEREE 1

General comments

- Tide gauges do not typically report instantaneous water level measurements. Instead, tide gauges average water level values sampled at a higher rate (than the data output rate). Therefore, downsampling the numerical mareograms every minute (line 190) does not produce an equivalent signal to the tide gauge (averaged) recording. Moreover, the sampling period typically corresponds to the output signal period, thus introducing a time shift of typically half the sampling period. These factors should be taken into account in the inversion and should lead to different results.

Thank you for the comment, we did not express this concept well in the article. Time series of the tsunami were saved at a sampling rate higher than 1 minute. As the tide gauge data present a sampling of one value per minute, we decided to resample the synthetic signal to the observed data sampling rate. The resampling has been made through a linear interpolation with python.

- The choice of including the Kasos tide gauge signal in the source inversion or not is not straightforward since the signal to noise ratio is so low. Fig. 8e-g show that particularly for the first 2-3 waves (up to minute 44), the signal to noise ratio is about 1 to 1. Lines 210-215 of the manuscript explain how the Kasos tide gauge signal is assigned a smaller weight, but still its inclusion is questionable when the quality of the recorded data is so poor. Adding random noise with a higher percentage of the clean synthetic waveform amplitude variance to the Kasos tide gauge in the test of Section 2.4 should provide an estimate of how much the low signal to noise ratio of the Kasos tide gauge affects the inversion results.

This is true. Accepting this suggestion, we modified the inversion procedure by excluding the signal recorded at Kasos tide gauge station. The results do not differ significantly from the previously presented calculation, underlining that this station, located in the far-field, does not significantly constrain the tsunami source for this specific event. However, we used the tsunami forward modeling at Kasos station as an independent verification of the tsunami source estimated through the inversion of the Ierapetra waveform.

Figure 4, 5, 6, 7, 8, 9 and **Table 2** are updated according to this modification. The changes are neither significant nor appreciable, in particular as regards the waveform signals.
Figure 10 has been removed, as Kasos station is no more included in the source inversion.

Kasos signals remain instead in **Figure 7** and **Figure 11** (that now becomes **Figure 10**), as they are just reported as predicted waveforms.

We also added in the supplementary material file the results obtained assigning to the Kasos station a weight that is 1/5 the Ierapetra one.

- Lines 190-191: The authors state that "We assumed linearity of the slip amount and the tsunami to obtain the scenarios for different slip values". Tide gauges, unlike deep water pressure sensors typically used for linear source inversions, are located in the nearshore where waves are clearly nonlinear. I'm having trouble believing that the linearity assumption is valid without testing it at each (tide gauge) location where it is used. Since the linearity assumption is key to the slip inversion, the authors should include a separate subsection in section 2 where the linearity assumption is verified.

Thanks for this comment, that is an important point in the methodology; now we verified the slip linearity assumption. Using a set of source parameters, we modelled the tsunami waveform at Ierapetra considering some different slip values, smaller and larger than unity; then we normalized the synthetic waveforms to be associated to the same slip value. The results show that the difference between the waveforms (the target simulated with a unitary slip and the one simulated with a different slip value and renormalised) is less than 5% of the target signal. Now we report the test in the supplementary material: both the unitary slip, the edges of the slip interval adopted in the inversion procedure are considered. We modified the main text (section 2.2) accordingly.

- The wave period of this particular tsunami is relatively small (2-5 min), and water depth values at the source region reach ~3000-4000 m. Thus, wave energy in the source region is certainly contained in the intermediate (kh~1) water range (outside the kh<π/10 shallow water range). Since a shallow water model was used, frequency dispersion was not considered per se in this study. Early wave arrival of the Green's functions is considered in the form of a time shift together with the inaccuracies of the bathymetry etc, but considering frequency dispersion in the form of a fixed time shift is not equivalent to resolving frequency dispersion through higher order terms in the governing equations. This is an epistemic uncertainty that can be alleviated with the use of a dispersive model, although such an undertaking would be very computationally demanding for such a large number of simulations. A short discussion on the effect of frequency dispersion for this particular (small) tsunami event should at least be included in the Data and Methodology section.

Thanks for the comment. Dispersion effects are not considered in the shallow water governing equations solved by Tsunami-HySEA code to numerically model the tsunami wave in our study. The tide gauge station (Ierapetra) used to estimate the tsunami source is located sufficiently near to the source, about 80 km; for such a distance, we assume the effects due to dispersion are negligible. This is consistent with the results presented in a recent study by Sandanbata et al. (2021), now cited in the revised version of our manuscript. They analysed how much dispersion and some additional factors, that reduce the tsunami speed, affect short-period tsunamis with dominant periods below ~1000 s. Their simulation results demonstrated that effects of these additional factors are negligibly small at stations up to ~500 km away from the source, whereas the effects appear as an apparent traveltime delay of ~40 s at a station ~1430 km away from the source. Even if considering a delay of such quantity (and it would not be the case for a near-source station as the one we analyze), it would be smaller than the sampling rate of the data and anyway included in the uncertainty assumed in the estimated delay.

Moreover, although the depth near the hypocentre can be high (about 3 km), it reaches a value of 1 km just after 20 km in the direction of the recording station, and then decreases in the remaining 60 km of propagation.

Heidarzadeh et al. (2021), studying the same tsunamigenic event, also assumed the dispersion effects as negligible, justifying the assumption with the fact that the tsunami wavelength is large enough for this approximation.

Now we modified section 2.2 in the main text accordingly.

- The source rupture area was fixed and the slip magnitude was varied in the source inversion. Also, the authors did not use the seismic moment as a constraint to try different combinations of rupture length, width and slip magnitude. I believe that was done to save computation time since the slip magnitude was accounted for as a linear perturbation of the Green's functions. The use of scaling laws to compute the fault rupture area and derive the initial conditions for the hydrodynamic simulations does not guarantee an agreement with the tsunami recordings. While in this case the authors produce an excellent agreement with the Ierapetra tide gauge recording, I'm not sure whether other source parameter combinations can produce equally good results. The expected implications in the inversion of using scaling laws to fix the rupture length and width should be briefly discussed after line 129.

The comment is more than legitimate. We decided for a fixed fault size due to the symmetry of the problem, in terms of source size and source position relative to the recording station, that does not allow to constrain the size of the fault along strike direction. There surely can be other combinations that could fit the data equally well because of this symmetry (as mentioned now in section 3). Due to the lack of such constraints, we imposed the source size (length and width) as fixed parameters. We have decided to use Leonard (2014; LE14) relations because they are derived from seismic moment and suitable for a crustal event. We have also evaluated the fault size using other scaling relations, such as WC94 (Wells and Coppersmith 1994) and TH17 (Thingbaijam et al. 2017). The differences are quite small (11% of Length between LE14 and TH17 and 18% of Width between LE14 and WC94) and even smaller if the source area is considered. We believe that these differences are fully absorbed by the variability of the other parameters, in particular the slip for moment variations, and the hypocentre position to cover a different coseismic deformation location.

Now, we clarify this point in section 2.1.

Technical corrections

- “tide-gauge” should be written as “tide gauge”.

Done.

- Line 77: Ebeling et al. (2012) is another reference for the 1948 earthquake and tsunami event:

Ebeling, C.W., Okal, E.A., Kalligeris, N. and Synolakis, C.E., 2012. Modern seismological reassessment and tsunami simulation of historical Hellenic Arc earthquakes. Tectonophysics, 530, pp.225-239.

Added, thank you.

- Line 119: use “topography-” instead of “topo-…”.

Corrected.

- Lines 162:163: describe the model governing equations in addition to the numerical scheme.

The model governing equations are now mentioned in the text (non-linear shallow water equations).

- Lines 172-173: the nautical charts the authors refer to were produced by the Hellenic Hydrographic Service. The issue date of the nautical charts used should also be mentioned in the text because it is an important piece of information.

Done.

- Lines 222-226: this is a difficult concept which I did not fully grasp and I believe needs to be explained/presented better.

True. It was not explained correctly. Now, even removing the Kasos signal from the inversion, it should be clearer.

- Line 237: what is the definition of ||aj|| here? The square root of the sum of the squares of all (seven) parameters?

It is. I added this specification to the main text.

- Line 270: it was not immediately clear to me what "resolution test results presented in Section 2" refers to. Better refer to them using the title of section 2.4, i.e. synthetic test.

Done.

- Lines 338-339: difficult to read. Sentence needs to be rewritten.

Done.

- Line 342: "The choice…is not sufficient for discriminating…" needs to be rephrased.

It was rephrased.

- Lines 397-398: the moment magnitude values resulting from the inversions can also be presented in Table 2.

Done.

- Figure 11: What is the sampling period of the W and HG numerical mareograms plotted here? Also, it is difficult for the reader to distinguish the magenta from the red curves.

The W and HG signals were also resampled to the observed data sampling rate (1 minute) through the same linear interpolation procedure adopted for our synthetic waveforms.
The magenta line was replaced by a black one.

ANSWERS TO REFEREE 2

1. **72 "Guidoboni and Comastri, 1997". Wrong citation, those authors reported on the 1303 tsunami not on the 365 one. Suggested citations for the 365 earthquake and tsunami are, among others, the books by Ambraseys (2009) and Papadopoulos (2011).**

   Thank you, corrected.

2. **75. Papadopoulos et al., 2014. The correct citation is Papadopoulos et al., 2012 (see reference).**

   Thank you, corrected.

3. **139. "a steep south-dipping plane". Please say a few words that may support from geotectonic point of view the possibility of considering such a type of fault in that area.**

   The arguments are reported in the discussion section.

4. **337 "Both synthetic signals reproduce quite well the first oscillations". Please mention how many sec are covered by the first oscillations, up to ~30 sec?**

   About 15 minutes, now it is mentioned in the main text.

5. **381 "not too distant from the source". It is better saying "in the near-field domain"**

   Corrected.

6. **492-493 "leaves very little time for warning". This operationally critical point was examined in details by Papadopoulos et al. (2020) as regards the 2 May 2020 seismic tsunami.**

Figure 1. Please draw an inset to show the region where the study area is situated.

The inset was added to Figure 1.

IN THE FOLLOWING PAGES, THE REVISED MANUSCRIPT IS REPORTED WITH THE MODIFICATIONS HIGHLIGHTED IN YELLOW FOR REFEREE 1 COMMENTS, AND GREEN FOR REFEREE 2 COMMENTS.

Characterisation of fault plane and coseismic slip for the May 2, 2020, Mw 6.6 Cretan Passage earthquake from tide gauge tsunami data and moment tensor solutions

Enrico Baglione[1,2], Stefano Lorito[2], Alessio Piatanesi[2], Fabrizio Romano[2], Roberto Basili[2], Beatriz Brizuela[2], Roberto Tonini[2], Manuela Volpe[2], Hafize Basak Bayraktar[3,2], Alessandro Amato[2]

[1]Istituto Nazionale di Oceanografia e di Geofisica Sperimentale (OGS)- Sgonico (TS) – Italy
[2]Istituto Nazionale di Geofisica e Vulcanologia, Sezione di Roma 1, Via di Vigna Murata 605, 00143, Roma, Italy
[3]Department of Physics "Ettore Pancini", University of Naples Federico II, Naples, 80126, Italy

Correspondence to: Enrico Baglione (enrico.baglione@ingv.it)

Abstract. We present a source solution for the tsunami generated by the Mw 6.6 earthquake that occurred on May 2, 2020, about 80 km offshore south of Crete, in the Cretan Passage, on the shallow portion of the Hellenic Arc Subduction Zone (HASZ). The tide gauges recorded this local tsunami on the southern coast of Crete Island and Kasos island. We used Crete tsunami observations to constrain the geometry and orientation of the causative fault, the rupture mechanism and the slip amount. We first modelled an ensemble of synthetic tsunami waveforms at the tide gauge locations, produced for a range of earthquake parameter values as constrained by some of the available moment tensor solutions. We allow for both a splay and a back-thrust fault, corresponding to the two nodal planes of the moment tensor solution. We then measured the misfit between the synthetic and the Ierapetra observed marigram for each source parameter set. Our results identify the shallow steeply-dipping back-thrust fault as the one producing the lowest misfit to the tsunami data. However, a rupture on a lower angle fault, possibly a splay fault, with a sinistral component due to the oblique convergence on this segment of the HASZ, cannot be completely ruled out. This earthquake reminds us that the uncertainty regarding potential earthquake mechanisms at a specific location remains quite significant. In this case, for example, it is not possible to anticipate if the next event will be one occurring on the subduction interface, on a splay fault, or on a back-thrust which seems the most likely for the event under investigation. This circumstance bears important consequences because back-thrust and splay faults might enhance the tsunamigenic potential with respect to the subduction interface due to their steeper dip. Then, these results are relevant for tsunami forecasting both in the framework of the long-term hazard assessment and of the early warning systems.

1 Introduction

On May 2, 2020, at 12:51:07 UTC, a strong earthquake occurred in the Cretan Passage, about 80 km offshore to the south of Crete Island in the eastern Mediterranean. According to the revised moment tensor solution distributed by the GEOFON (https://geofon.gfz-potsdam.de/), the earthquake was located at 25.75°E and 34.27°N, at a depth of 10 km, and the moment magnitude (Mw) was 6.6 (Figure 1). Within about 10-15 minutes after the event, estimates of the earthquake magnitude varied from Mw 6.5 to 6.7. This appears, for example, from tsunami alerts issued by the three Tsunami Service Providers (TSPs) of the Tsunami Early Warning and Mitigation System in the North-eastern Atlantic, the Mediterranean and connected seas (NEAMTWS, http://www.ioc-tsunami.org/), in charge for monitoring this region: the Centro Allerta Tsunami - Istituto Nazionale di Geofisica e Vulcanologia (CAT-INGV), the National Observatory of Athens (NOA), and the Kandilli Observatory and Earthquake Research Institute (KOERI). These estimates were then confirmed by the moment tensor solutions which started to appear immediately after (Figure 2a).

The 2020 Cretan Passage earthquake generated a local tsunami along the south-eastern coast of Crete, as reported by eyewitnesses and local authorities and documented by a series of pictures and video shootings taken by authorities, press, and amateurs at Arvi and Kastri villages (Papadopoulos et al., 2020). The NOA-04 tide gauge station, located in the port of Ierapetra, recorded a peak-to-trough excursion exceeding 30 cm, with a positive peak amplitude of about 20 cm recorded 23 minutes after the earthquake origin time, with a wave period of ~3.5 minutes. Small tsunami waves (less than 10 cm peak-to-trough) were also recorded at the NOA-03 tide gauge, located in the Kasos Island, where the peak amplitude of 5 cm was recorded at 13:53 UTC, and the wave period was estimated to be 8 minutes by Papadopoulos et al. (2020) and 4.5 minutes by Heidarzadeh and Gusman (2021). As in the Mw 6.4, July 1, 2009, event (Bocchini et al., 2020), the tsunami was also observed in the Chrysi islet (located offshore south of Ierapetra), where no tide gauges are operating. No casualties, injuries or damage were reported due to the tsunami.

The 2020 Cretan Passage earthquake occurred in the Hellenic Arc Subduction Zone (HASZ). The HASZ is the active plate boundary that accommodates the convergence of the African (or Nubia) plate sinking under the Aegean plate. The arc stretches NW-SE from Kefalonia-Lefkada to Crete and SW-NE from Crete to Rhodes. According to GPS velocities, the relative motion across the HASZ is ~30 mm/y in the NE-SW direction (Nocquet, 2012). The HASZ is characterised by an active volcanic arc in the southern Aegean Sea, an outer non-volcanic arc marking the transition from back-arc extension to contraction in the forearc along the Ionian Islands, Crete, and Rhodes (backstop), a complex accretionary wedge characterised by alternating forearc basins, known as part of the Hellenic Trench (or Trough) System (Matapan, Poseidon, Pliny, and Strabo basins, Fig. 1) and Inner Ridges, and the more external, thicker, and wider, Mediterranean Ridge. The accretionary wedge extends above the oceanic crust for more than 200 km, with its leading-edge affecting the remaining abyssal plains (Ionian, Sirte, and Herodotus) and nearing the African continental margin (Polonia et al., 2002; Kopf et al., 2003; Chamot-Rooke et al., 2005;

Yem et al., 2011) and has an outward growth rate of 5-20 mm/y (Kastens, 1991). According to reconstructions based on seismic reflection data, most of the structural characteristics of the Mediterranean Ridge external domain can be explained by the presence of thick Messinian evaporites, whereas the internal structures include both frontal thrusts and back-thrusts (Chaumillon and Mascle, 1997; Kopf et al., 2003). Back-thrusts mainly characterise the transition of the Mediterranean Ridge to the inner domain. Strike-slip motions are also present within the Hellenic Trench system.

Several strong earthquakes struck this area in the past. The largest documented earthquake is the Mw~8.3 365 CE event that occurred in the central forearc of the subduction zone southwest of Crete (Papazachos et al., 2000; Papazachos and Papazachos, 2000; Stiros, 2001). This earthquake generated a devastating tsunami (Guidoboni et al., 1994; Ambraseys, 2009; Papadopoulos, 2011). Another remarkable event is the Mw~8 earthquake of August 8, 1303, which occurred southeast of Crete Island, specifically in the arc portion between Crete and Rhodes (Guidoboni and Comastri, 1997, Papazachos, 1996). This earthquake was probably the cause of a tsunami that affected Alexandria in Egypt (Guidoboni and Comastri, 1997). Other strong tsunamigenic earthquakes in the easternmost Hellenic Arc are the Mw 7.5, May 3, 1481 event (Yolsal-Çevikbilen and Taymaz, 2012) and the Mw 7.5, January 31, 1741 (Papadopoulos et al., 2007) one. The occurrence of the 1303, 1481 and 1741 tsunamis is also geologically testified by sediments found on the Dalaman coast (Papadopoulos et al., 2012). Another large tsunamigenic earthquake (M ~ 7.0–7.5) occurred near southern Crete on July 1, 1494 (Yolsal-Çevikbilen and Taymaz, 2012). More recently, an earthquake of Mw 7.5 occurred on February 9, 1948, near the coast of Karpathos, on the Pliny Trench (Papadopoulos et al., 2007, Ebeling et al., 2012) and, on July 1, 2009 (UTC 09:30), a moderate earthquake (Mw 6.5) located in the southern offshore margin of Crete caused a local tsunami of about 0.3 m of wave height (Bocchini et al., 2020).

Despite the relatively high seismicity documented by decades of investigations in macroseismic and instrumental historical seismology in the eastern Mediterranean, several aspects of the tectonic and geodynamic processes that characterise the Hellenic forearc deserve further investigations. For example, the transition from extension to contraction in the forearc is not well delimited, and even the type of seismogenic activity at the subduction interface is not entirely clear.

For example, the great 365 CE earthquake has been associated with different crustal faults in the upper plate: a reverse splay fault (Shaw et al., 2008; Shaw and Jackson, 2010; Saltogianni et al., 2020) and, recently, a pair of orthogonal normal faults (Ott et al., 2021). Conversely, it seems that the 1303 event was due to a rupture on the plate interface itself (Papadopoulos, 2011; Saltogianni et al., 2020). Two recent earthquakes that occurred near the 2020 Cretan Passage event were attributed to two different mechanisms. The source of the recent Mw 6.5, July 1, 2009, earthquake that triggered a small tsunami was suggested to be a splay fault (Bocchini et al., 2020). The Mw 5.5, March 28, 2008, earthquake that occurred to the south of Crete was instead attributed to a north-dipping low-angle thrust faulting mechanism with a small amount of left-lateral slip component (Shaw and Jackson, 2010; Yolsal-Çevikbilen and Taymaz, 2012) representing the subduction interface.

Although all the envisaged mechanisms of these examples are consistent with the variety of mechanisms that characterise a subduction zone, the study of the seismogenic and tsunamigenic sources south of Crete remains of key importance for improving the characterisation of the associated hazards, which affects the nearby inhabited coastal areas. This region was already identified as subject to relatively high seismic and tsunami hazard (e.g., Sørensen et al., 2012; Woessner et al., 2015; Basili et al., 2021), and a better characterisation of the potential sources may reduce the uncertainty of such estimates.

Other authors have already studied the 2020 Cretan Passage event. In particular, Heidarzadeh and Gusman (2021) studied the tsunami source and obtained a heterogenous slip model by inversion and spectral analysis of the tsunami records. They impose a fixed fault geometry for their model, that is one of the two nodal planes (strike, 257°; dip, 24°; rake 71°) of the GCMT solution (Dziewonski et al., 1981; Ekström et al., 2012). This solution is a north-dipping plane compatible with a dominantly thrusting mechanism on a splay fault. The fault centre is placed roughly in the middle between the United States Geological Survey (USGS) epicentre (25.712° E, 34.205° N) and the GCMT centroid location (25.63° E, 34.06° N).

Here, we invert tsunami data for the fault location and orientation (strike and dip angles) as well as for the earthquake-average slip amount and direction (rake angle). To limit the solutions to be explored, we first constrain the parameters to range around the values of the available moment tensor solutions. In this way, while focusing on solutions compatible with the moment tensor inversions of seismic data, we do not exclude a priori that the earthquake might have happened on either nodal planes of these mechanisms. Then, we produce the synthetic tsunami waveforms at the Ierapetra and Kasos tide gauges for all the sources we obtained. Lastly, we calculate the misfit with Ierapetra observed signal, analyse the misfit distribution for the whole ensemble of models explored, and derive the most likely source model for this earthquake.

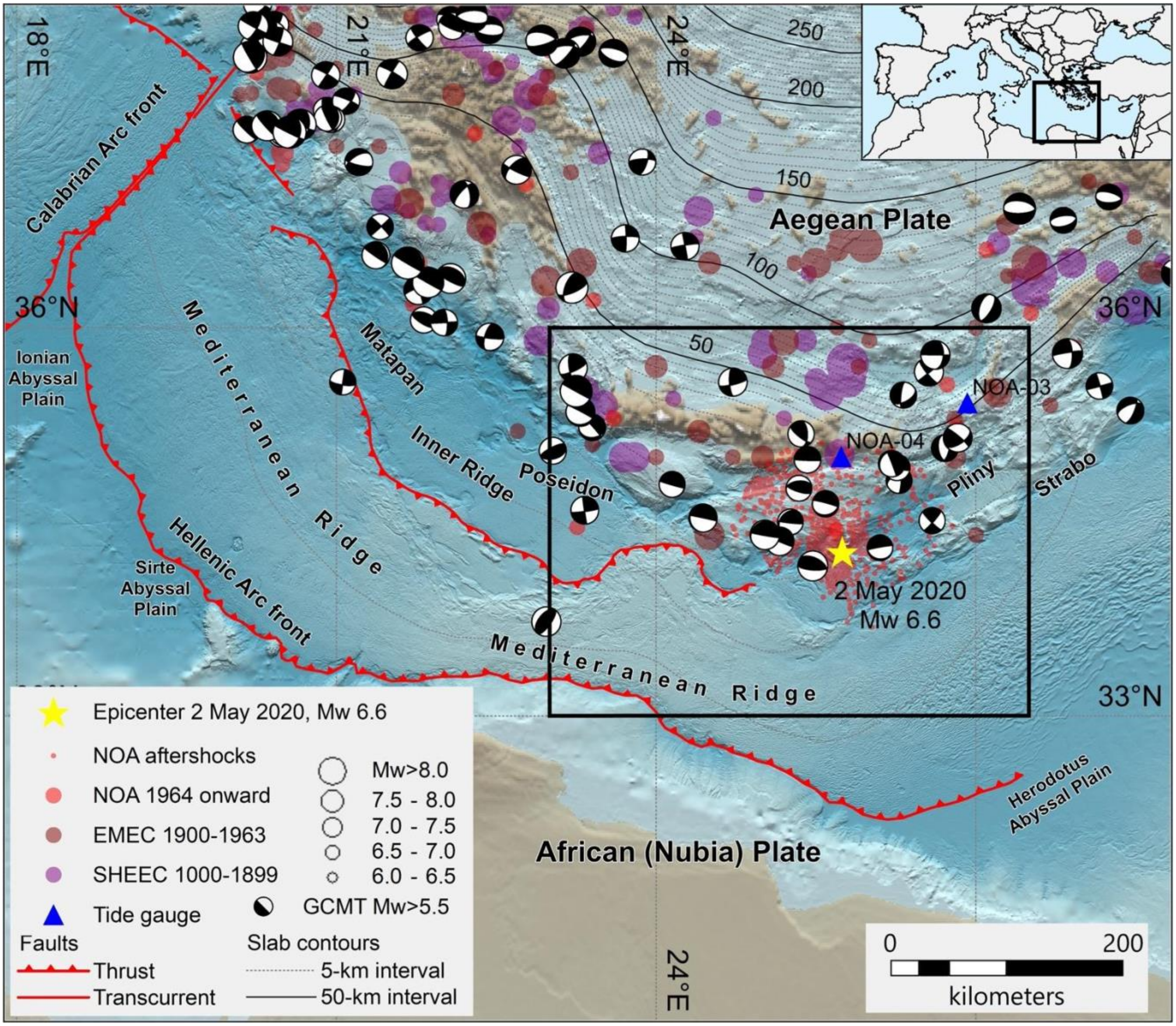

Figure 1: Main seismotectonic elements of the Hellenic Arc Subduction Zone (HASZ). The seismicity is derived by the SHEEC-EMEC (Grünthal and Wahlström, 2012; Stucchi et al., 2013) and NOA (http://www.gein.noa.gr/en/seismicity/earthquake-catalogs) earthquake catalogues. Focal mechanisms are from the Global Centroid Moment Tensors database (GCMT; Dziewonski et al., 1981; Ekström et al., 2012). The slab depth contours are resampled from the European database of Seismogenic Faults (EDSF) (Basili et al., 2013). The topography-bathymetry is obtained by splicing the ETOPO1 Global Relief Model and EMODnet Digital Bathymetry (DTM 2020) (NOAA, 2009; Amante and Eakins, 2009; EMODnet Bathymetry Consortium, 2020). The inset shows the location of this map and the black rectangle outlines the area shown in Figure 2a.

2 Data and Methodology

We compared the sea level observations at the Ierapetra tide gauge with the synthetic waveforms obtained through numerical tsunami simulations, to identify the source that produced the tsunami based on many different sets of fault parameters. In this section, we describe the technical details of our approach.

2.1 Seismic source parameterization

The symmetry of the problem, in terms of source size and position relative to the Ierapetra tide gauge, does not allow to constrain the size of the fault along strike direction; thus, we adopted a fixed source size. We use a rectangular fault with uniform slip, where length and width were assigned based on earthquake scaling relations (Leonard, 2014) for a fixed moment magnitude Mw = 6.6. We also varied position, depth, strike, dip, rake, and slip, testing different combinations of source parameters for a total of 41,310 solutions (Table 1).

The earthquake struck in a region where hypocentral locations are usually poorly constrained (Bocchini et al., 2020). The use of a different number of seismic stations, the type of phases used (namely at local, regional or teleseismic distances) and the choice of velocity models can lead to a significant discrepancy in hypocentral locations. The centre of the rectangular fault is thus allowed to span different values of latitude, longitude, and depth (Table 1) to consider this variability.

Strike, dip, and rake are explored by regular steps within a range of values that envelopes the focal mechanism solutions provided by several agencies (GFZ, USGS, GCMT, IPGP; Figure 2a). Two classes of nodal planes are explored; one is a north shallow-dipping plane, coherently with the dip direction of the subduction interface in that region, or a splay fault (hereafter called "plane S"), the other one is a steep south-dipping plane, likely identifying a back-thrust ("plane B"). Some "extreme" values, like a dip larger than 70° for plane B or lower than 20 for plane S, have been excluded after some preliminary tests, as they were significantly worsening the misfit between synthetic and observed waveforms. Slip is allowed to vary between 0.35 and 1.15 m, with a step of 0.05 m.

Table 1: Source parameters variability of the source model dataset for the tsunami simulations. The different sets of focal plane parameters are separated by parenthesis (B and S refer to the back-thrust and splay fault solutions). Positions and depths are referred to the centre of the fault plane.

Source parameters	
Length (km)	26.04
Width (km)	15.42
Depth (km)	10; 15; 20
Lat (°N)	34.1; 34.2; 34.3
Lon (°E)	25.6; 25.7; 25.8

Slip (m)	from 0.35 to 1.15, step 0.05
Strike (°)	B (95; 105), S (225; 235; 245; 255; 265)
Dip (°)	B (50; 60; 70), S (20; 30; 40)
Rake (°)	B (85, 95; 105; 115, 125), S (45; 55; 65; 75)

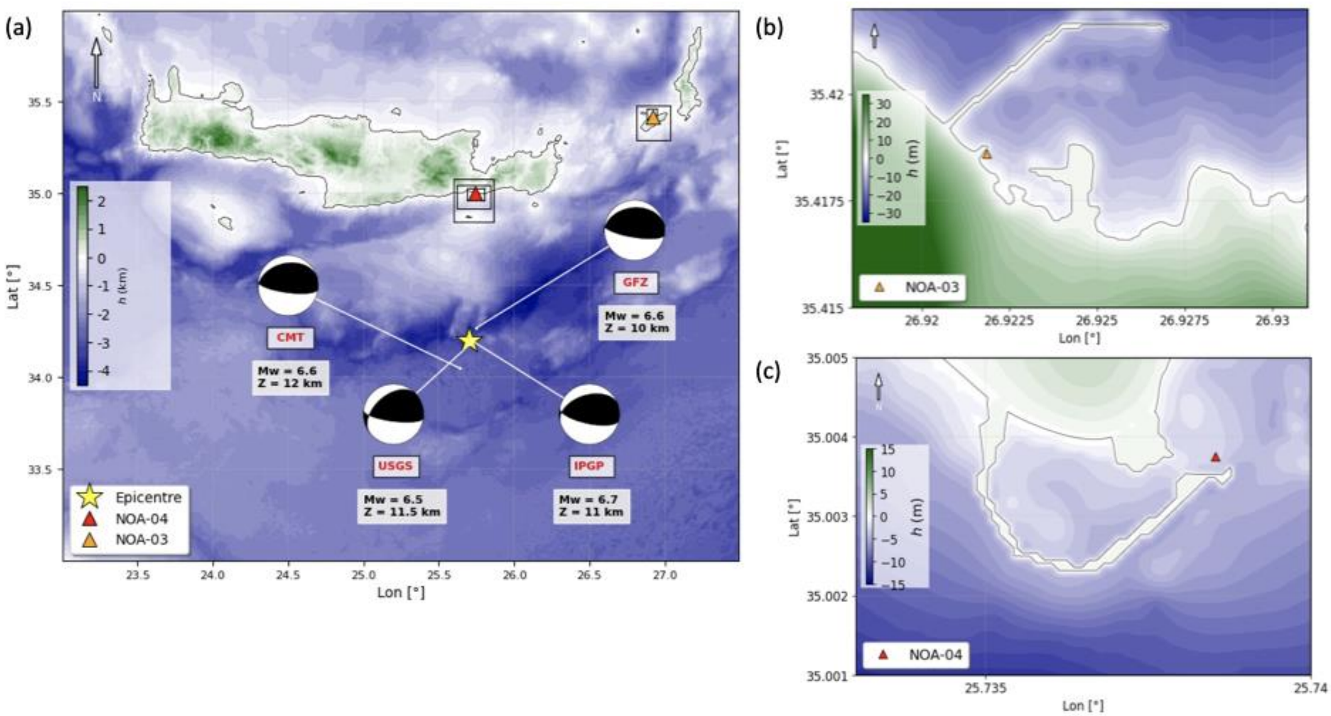

Figure 2: (a) Computational domain for the tsunami modeling adopted in this study (see text for details). The yellow star indicates the epicentre, at the centre (34.2°N, 25.7°E) of its considered variability range. THe different bathymetric levels are plotted as black rectangles. The red and orange triangles represent the Ierapetra (NOA-04) and Kasos (NOA-03) tide gauge stations, respectively. The different focal mechanisms used as reference values to let the inversion parameters vary are plotted, each with its own agency label: GEOFON (GFZ, https://geofon.gfz-potsdam.de/), United States Geological Survey (USGS, https://earthquake.usgs.gov/), Institut de Physique du Globe de Paris (http://geoscope.ipgp.fr/), Global CMT Catalog (https://www.globalcmt.org/). (b) High-resolution bathymetry data (10 m spatial resolution) around NOA-03 (Kasos) and (c) NOA-04 (Ierapetra) tide gauges.

2.2 Tide gauge data and tsunami modelling

The tsunami signal recorded by the tide gauges at Ierapetra (NOA-04) and Kasos (NOA-03) was obtained after removing the tidal component from the original waveform (http://www.ioc-sealevelmonitoring.org, sampling rate of 1 min) through a LOWESS procedure (e.g., Romano et al., 2015).

Tsunami numerical modelling was performed with the Tsunami-HySEA software, which solves non-linear shallow water equations using a finite volumes approach and a nested grid scheme to progressively increase the resolution during the propagation from the source to the tide gauges.

The software has undergone proper benchmarking (Macías et al., 2017) according to the community standards (e.g., Synolakis et al., 2009), also within the framework of the US tsunami hazard program (http://nws.weather.gov/nthmp/). The code is implemented in CUDA (Compute Unified Device Architecture) and runs in multi-GPU architectures, yielding remarkable speedups compared to other CPU-based codes (de la Asunción et al., 2013).

Dispersion effects are not considered in the governing equations and, thus, not modelled. Nevertheless, we have assumed acceptable this approximation because the main tide gauge station (Ierapetra) is located sufficiently near to the source (about 80 km). For such a distance, and for a relatively small source, even if the waveform period is relatively short (~5 min), we assume the effects due to the dispersion are negligible (see Sandanbata et al., 2021; Heidarzadeh et al., 2021).

To build the bathymetric and topographic grid models for the simulations, we used: 1) the European Marine Observation and Data Network (EMODnet) project database (EMODnet DTM version released in 2018, http://portal.emodnet-bathymetry.eu/), which has a resolution of about 115 m; 2) the European Digital Elevation Model (EU-DEM), version 1.1 (eu_dem_v11_E50N10), with a resolution of 25 m; and 3) the nautical charts (https://hartis.org/en) of Ierapetra harbour (Ierapetra Bay, 1:10,000 scale; Kaloi Limenes Bay, 1:12,500 scale, original version: 1962, with small corrections in the period 1964-2010) and Kasos harbour (Diafani Harbour, 1:5,000 scale; Pigadia Bay and Harbour, 1:5,000 scale; Emporio Harbours, 1:5,000 scale, original version 1998, with small corrections in the period 2000-2020). The computational domain (33-36° N, 23-27.5° E, Figure 2a) for tsunami propagation consisted in four levels of nested grids with increasing resolution approaching the Ierapetra and Kasos harbours (640, 160, 40, and 10 m, respectively). The domains of the finest grids are shown in Figures 2b and 2c.

The instantaneous seafloor vertical displacement was calculated using Volterra's formulation of elastic dislocation theory applied to a rectangular source embedded in an elastic half-space (Okada, 1992), and the initial velocity field is assumed to be zero everywhere. The initial sea surface elevation was obtained by applying a low-pass filter to reproduce the water column attenuation; the filter has a trend of the type 1/cosh(kh), where "k" is the wavenumber, and "h" is the average water depth (Kajiura, 1963).

We performed 2,430 simulations exploring all the source parameters (Table 1) except for the slip, which is fixed in all runs to 1 meter to obtain Green's functions. For all of these scenarios, we simulated one hour of propagation after the earthquake origin time (hereinafter OT) for the Ierapetra station and one hour and 30 minutes of propagation for the Kasos station. These simulation lengths allowed us to have about 50 minutes of tsunami signal at both gauges, which is more than enough to include the first tsunami oscillations (~30 min), that carry the information on the source and are used for the inversion (see Section

2.3). Time histories of the tsunami waves were calculated at the wet points of the computational grid closest to the Ierapetra and Kasos station coordinates (see Figure 2). The synthetic signals were resampled to the observed data sampling rate (1 per minute) through a linear interpolation. We assumed linearity between the slip amount and the tsunami to obtain the scenarios for different slip values. The assumption of slip linearity was preliminarily tested and verified (results are shown in the supplementary material).

Thus, we multiplied each of the computed marigrams by all the 17 slip values, for a total of 41,310 tsunami realisations.

2.3 Inversion

To retrieve the fault parameters and the coseismic slip simultaneously, we solved a nonlinear inverse problem. Since the number of sources in our ensemble is not very large, we opted for a systematic search of the parameters' space.

The comparison between the synthetic and the observed waveforms is carried out in the time domain. The misfit between the two waveforms is evaluated through a cost function frequently used to compare tsunami signals in source inversions (e.g., Romano et al., 2020):

$$E = 1 - \frac{\sum_{t_i}^{t_f} \eta(t-T)\eta_0(t)}{\sum_{t_i}^{t_f} \eta^2(t-T) + \sum_{t_i}^{t_f} \eta_0^2(t)}, \quad (1)$$

In equation (1) $\eta(t)$ and $\eta_0(t)$ are the synthetic and the observed waveforms, respectively, t_i and t_f are the lower and upper limit of the considered time window, and T is a time shift. The cost function considers both the amplitude and the shape of a waveform; it is more robust than a least-squares misfit, whose solutions are very sensitive to a small number of large errors in the dataset (Tarantola, 1987). For each combination of the source parameters, the cost function is minimised with respect to time shift values between -5 and 5 minutes, with one-minute steps. The arrival time optimisation is used to overcome the often found time alignment mismatch between the observed and modelled tsunami waveforms, with the latter generally arriving earlier. This approach was introduced by Romano et al. (2016), and the details are discussed further in Romano et al. (2020).

Kasos tide gauge is in the far field of the tsunami source (see Figure 2) and its signal-to-noise ratio is so low. After several preliminary tests, where both the tide gauge waveforms were inverted, we observed that the Kasos tide gauge was not significantly sensitive to constrain the tsunami source of the 2020 Cretan passage event. Therefore, we decided to use only the signal recorded at Ierapetra.

Time window of [5, 30] minutes after the earthquake OT is chosen. This choice was made to include the first tsunami oscillations, which are mainly driven by the seismic source. The remaining part of the records is not used for the inversion, because it is highly probable that other factors, such as the local propagation and the port structure, start to control the shape of the signal (Romano et al., 2016; Cirella et al., 2020). To quantify the relative importance of these factors, the cost function is also evaluated in the 25 minutes following the considered interval, that is in the time windows [30,55]. The average of the cost functions (E_1 for [5, 30], E_2 for [30,55]) is calculated from the 5, 10, 50, and 100 percent of models with the lowest misfit E_1 (within the first window used for the inversion) with the observed data. We observe that the ratio E_2 /E_1 significantly decreases when using progressively more models (E_2/E_1 = 9.9, 7.9, 3.9, 2.7, respectively). This observation confirms that the information about the source dominates the first intervals used for the inversion.

2.4 Synthetic test

We first investigated the resolution offered by the two stations using as a target source model all possible combinations of the source parameters $A(a_1, a_1, \ldots, a_n)$. These are the same models we explored in the inversion for the real case. For each of them we calculated the corresponding synthetic target waveform and corrupted it by adding a Gaussian random noise with a variance corresponding to the 10% of the clean waveform amplitude variance. A random time shift between -5 and 5 minutes is added to mimic the typically observed time mismatch between the observed and the predicted tsunami signals.

All the waveforms f(A) derived from all the possible source models are tested against each of these noisy and shifted target waveforms $f_T(A)$ using equation (1). We then defined the distance between two different models as:

$$d_{ij} = \frac{\|a_i - a_j\|}{M \cdot \|a_j\|}, \qquad (2)$$

Where a_i= (strike, dip, rake, slip, depth, lon, lat)$_i$, a_j= (strike, dip, rake, slip, depth, lon, lat)$_j$ are the parameters associated with the i-th (j-th) combination (||a|| is the square root of the sum of the squares of the parameters), and M (equal 7) is the number of free parameters.

For each target model a_i, the distance d is evaluated with respect to:

1) the best model a_{best}, whose $f(a_{best})$ presents the lowest cost function;
2) the average model a_{wm} evaluated as a weighted mean over the first 5% of the models with the lowest cost function, where the weights are chosen as the reciprocal of the cost function.

The result confirms that the tsunami data well constrain the seismic source process. In most cases, the target parameters correspond to those of the model which minimises the cost function (Figures 3a and 3c). Hence, the target focal plane is correctly identified. The few cases showing a high value of the distance occurs when the algorithm does not recognise if the target is a back-thrust or a splay fault.

On the one hand, when using the average model, the distance between the models almost never vanishes (Figures 3b and 3d), meaning that the target's parameters are not perfectly reproduced, as expected for an average model. On the other hand, the averaging process has the power to make the distribution smoother and unimodal and to eliminate or diminish the number of occurrences corresponding to a high distance. So, choosing the average over the best models may protect us from overfitting. Figure 3e shows that the B plane (a back-thrust) is much better spotted than the S one (the splay) by the best models; when using the average model, the difference in the "specificity" of the cost function is slightly reduced but still present (Figure 3f).

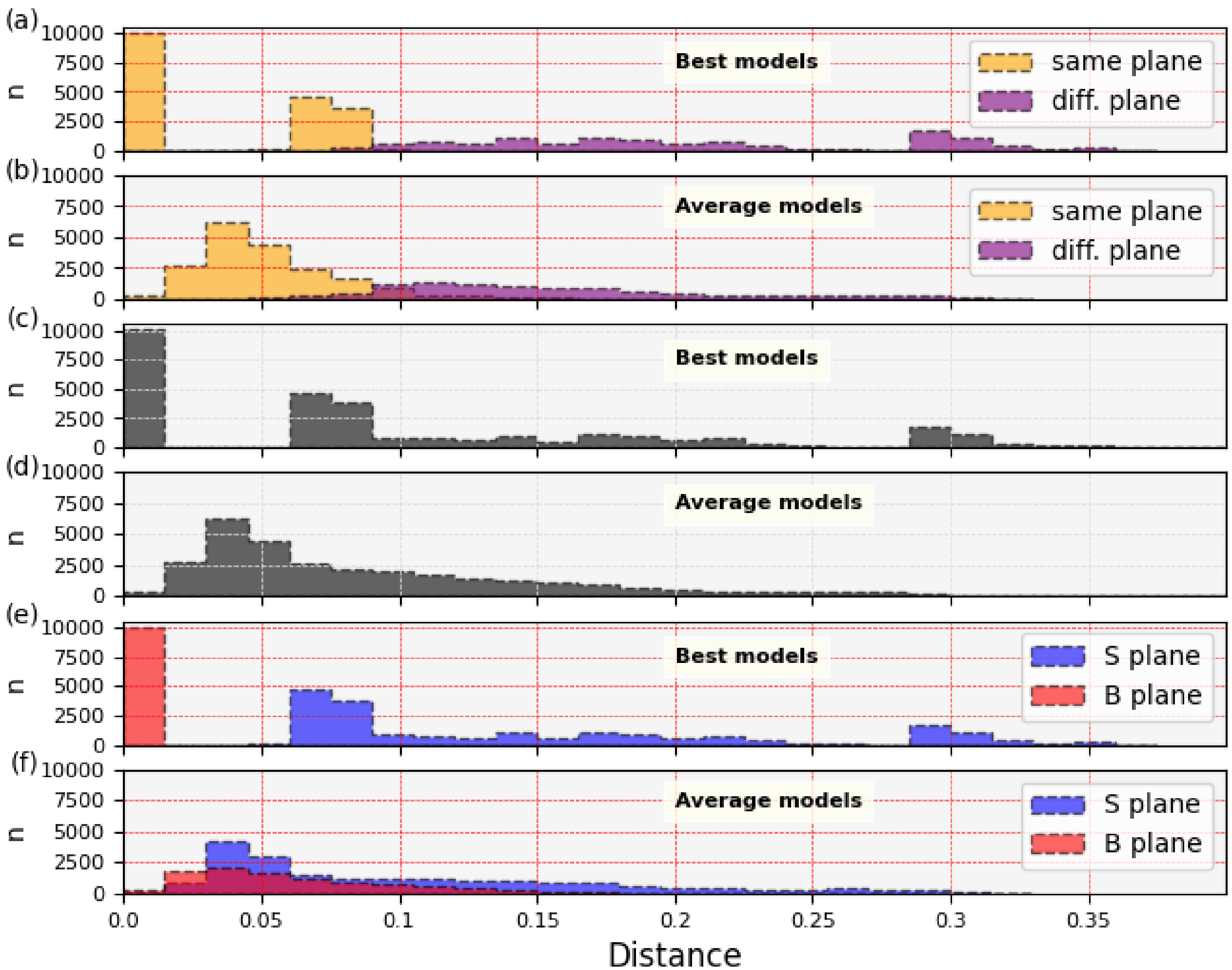

Figure 3: Distributions of the parameters distance for the best (a, c, e subplots) and average models (b, d, f subplots). Subplots (a) and (b) separate the models for which the target model focal mechanism is reproduced or not. Subplots (c) and (d) report all the models together. Subplots (e) and (f) separate the target models associated with the B (red) or S (blue) focal plane solutions.

3 Results of the application to the May 2, 2020, Mw 6.6 Cretan Passage earthquake

We performed the inversion using the observations at Ierapetra, the only near-source sea level recording available. The distribution of the cost function values for all the investigated models is shown in Figure 4. Figure 4a displays separately the cost function values obtained for the two focal solutions. Overall, the cost functions of the B plane are slightly lower than those of the S plane. However, the left portions of the distributions, that is the ones containing the models with the lowest misfit with respect to the observed marigrams, are almost overlapped. The same tendency can be seen in Figure 4b where the distribution has a slightly bimodal character with the two modes corresponding to the S and B planes, respectively.

Based on the resolution test results presented in the synthetic test, we evaluated the weighted average of the models included in the 5^{th} percentile of the cost function distribution for each focal solution (those to the left of the dashed lines in Figure 4a). We used as a weight the inverse of the cost function. Both the best and average models, as well as the associated errors obtained as weighted standard deviations, are reported in Table 2.

The average models, along with the associated errors, may indicate that the best model is ‘‘overfitting’’ the data. This happens, for example, when the best and average models are very different or when the uncertainties are very large. Standard deviations give a measure of the uncertainties in the estimation of the corresponding parameter. Smaller values of the standard deviation denote a parameters’ better resolution (Mosegaard and Tarantola, 1995; Sambridge and Mosegaard, 2002; Piatanesi and Lorito, 2007).

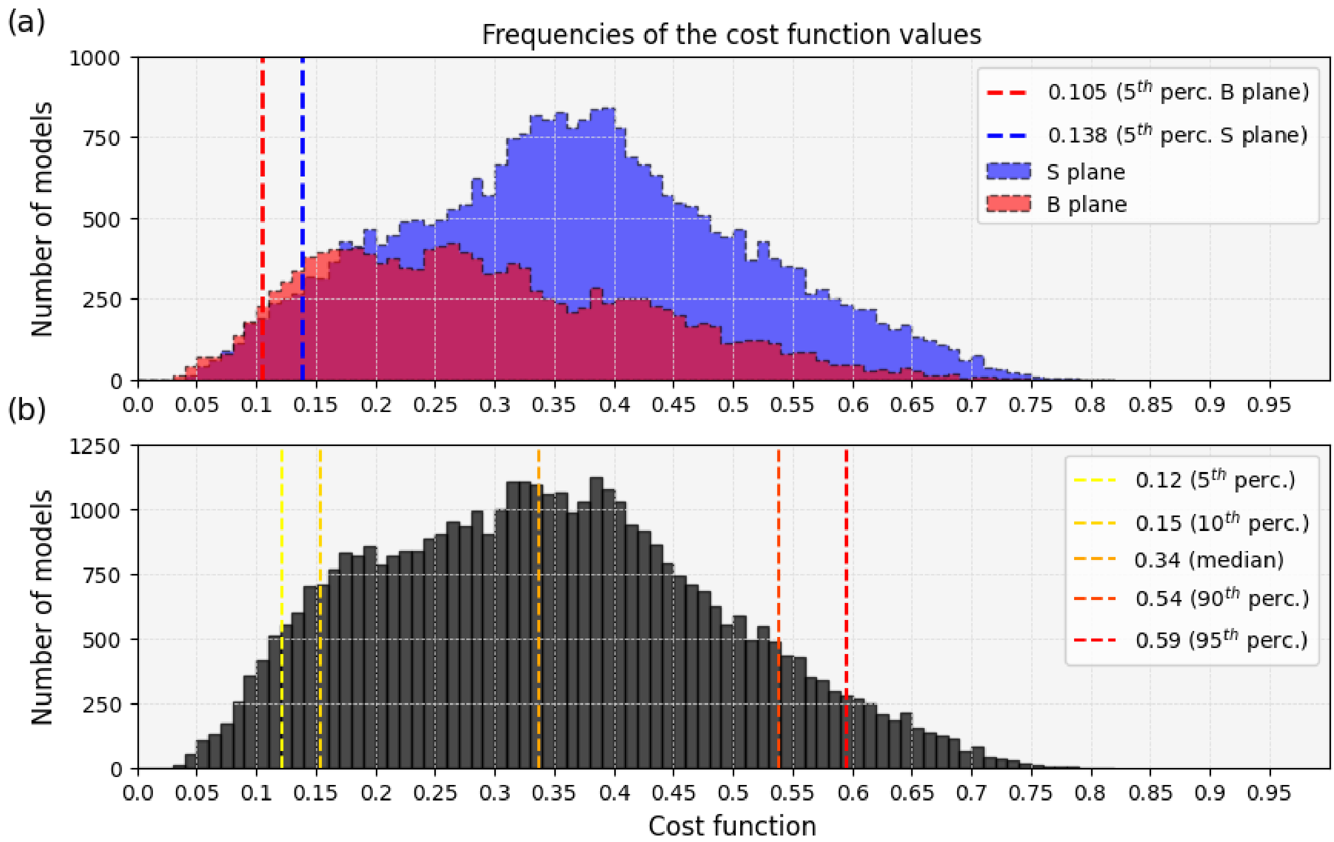

Figure 4: (a) Cost function distribution for the back-thrust (red) and the splay (blue) models; the vertical dashed lines indicate the 5th percentiles for each of the two focal solutions. (b) Histogram of the cost function values for all the models considered. The vertical dashed lines represent the 5th, 10th, 50th (median), 90th and 95th percentile.

With only a few exceptions, all the best model parameters fall within the range of one standard deviation from the average model. For both focal solutions, the slip of the best models is quite smaller than the average one and does not fall within the uncertainty limits.

The S plane solutions are centred about 10 km north of the B planes, slightly closer to the southern coast of Crete. Coherently, the predicted tsunami arrives earlier (i.e., the estimated time-shift is bigger) with respect to the waves resulting from the B plane solutions. The rake angle, both for B and S planes, presents a large dispersion. The same can be said for the strike associated with the S plane. On the other hand, the dip appears to be better constrained.

Table 2: Best and Average Model extracted from the models with the smallest cost functions within the 5th percentile. The percentiles refer to B and S planes separately (i.e., the models at the left of the red and blue vertical dashed lines in Figure 4a, respectively). B plane refers to the back-thrust solution dipping south; S plane refers to the splay fault dipping north. Lat, Lon and Depth refer to the centre of the fault.

	Best model plane B	Average model (5^{th}) plane B	Best model plane S	Average model (5^{th}) plane S
Depth (km)	10	13 ± 3	10	12 ± 2
Lat (°N)	34.1	34.17 ± 0.07	34.2	34.18 ± 0.07
Lon (°E)	25.7	25.72 ± 0.04	25.7	25.73 ± 0.06
Strike (°)	95	99 ± 5	255	250 ± 13
Dip (°)	50	53 ± 5	40	39 ± 2
Rake (°)	105	107 ± 14	75	64 ± 11
Slip (m)	0.50	0.64 ± 0.14	0.55	0.71 ± 0.16
Time shift (min)	1	1.6 ± 0.7	2	1.8 ± 0.7
Mw	6.5	6.6 ± 0.1	6.6	6.6 ± 0.1

Figures 5-7 help to visualise the parameter variability and how the best source models are characterised. The marginal (Figure 5) and the joint distributions (Figure 6 and 7) are provided for the two planes. Marginal and joint distributions provide an additional measure of the uncertainties. Narrower distributions suggest that the corresponding parameters are better resolved than those characterised by broader ones.

The strike angle for plane B and the dip angle for plane S show a strongly “preferred” value (diagonals of Figures 6 and 7). The rake angle does not show a real preferential value: evidently, we do not have enough precision to discriminate at this level of resolution. Plane B solutions are characterised by a larger depth dispersion and by a higher average depth value. However, the depth of 20 km almost never occurs, suggesting the occurrence of a shallow event. The slip shows a “bell-shaped” distribution with a peak at 0.60 m and 0.70 m for B and S plane respectively, and significant occurrences in the range 0.45-0.90; the best source slip is lower than the average, both for plane S and B. S plane solutions are characterised by a slightly higher slip than B plane solutions. There is a correlation between the slip and depth values: deeper solutions consistently feature a larger slip. In this case, a lighter correlation also exists between slip and latitude: events further south have a slightly greater slip, especially for B solutions. As regards the hypocentre determination, establishing a univocal position is not obvious, also because the delay adds a trade-off in constraining the hypocentre. Consequently, the Longitude is better constrained than the Latitude since the latter is more strongly correlated with the arrival time given the relative position of the tide gauges (both to the north) with respect to the source. The preferred longitude is 25.7°E, with fewer occurrences a little further east and almost none further west.

There surely can be other parameters combinations (length, width) that could fit the data equally well because of the problem symmetry discussed in Section 2.1. But, for the reasons mentioned above, we decided to fix the fault length and width, using Leonard relationship because they are seismic moment derived and suitable for a crustal event.

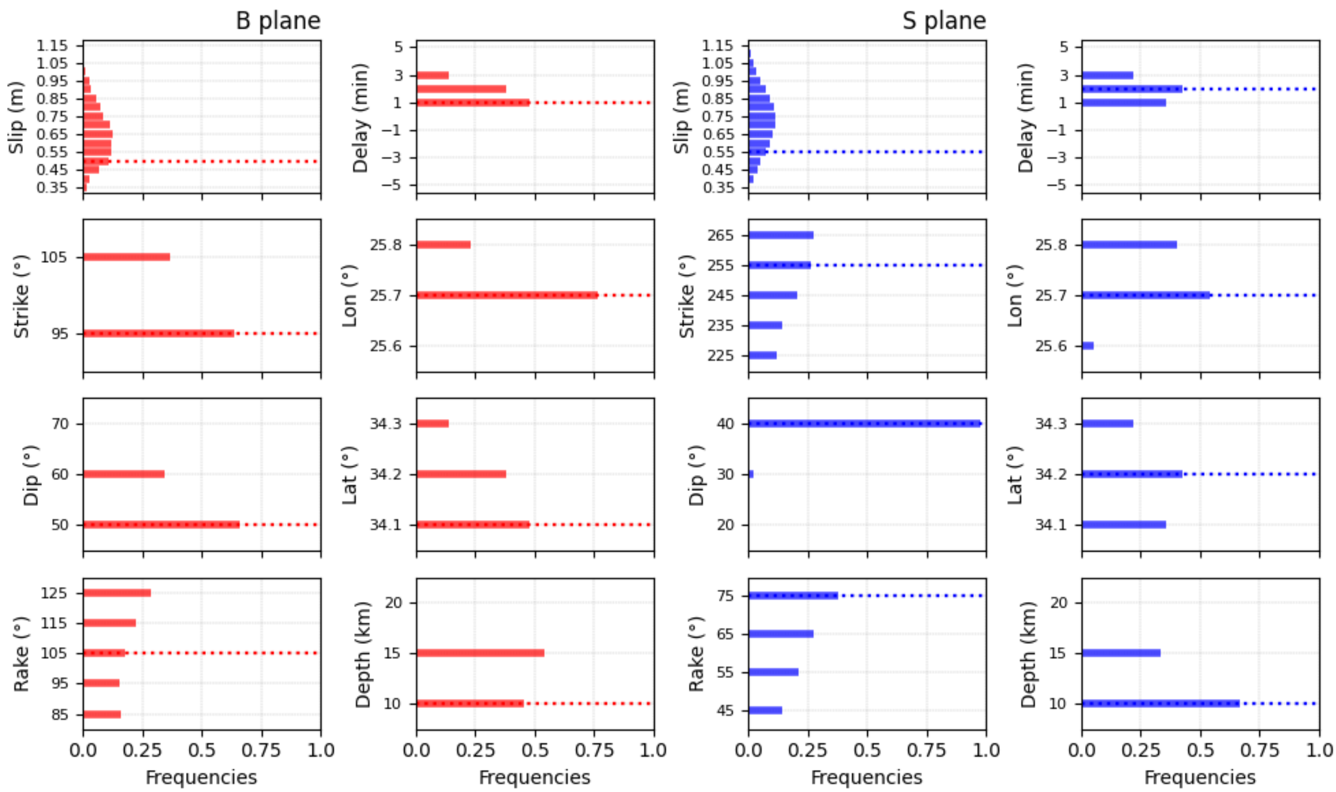

Figure 5: Marginal distributions for each of the inverted parameters, considering the first 5 percent of B (1st and 2nd columns) and S (3rd and 4th columns) plane models, those at the left of the red and blue vertical line in Figure 3a. The red and blue horizontal dotted lines mark the best models for the B and S planes, respectively.

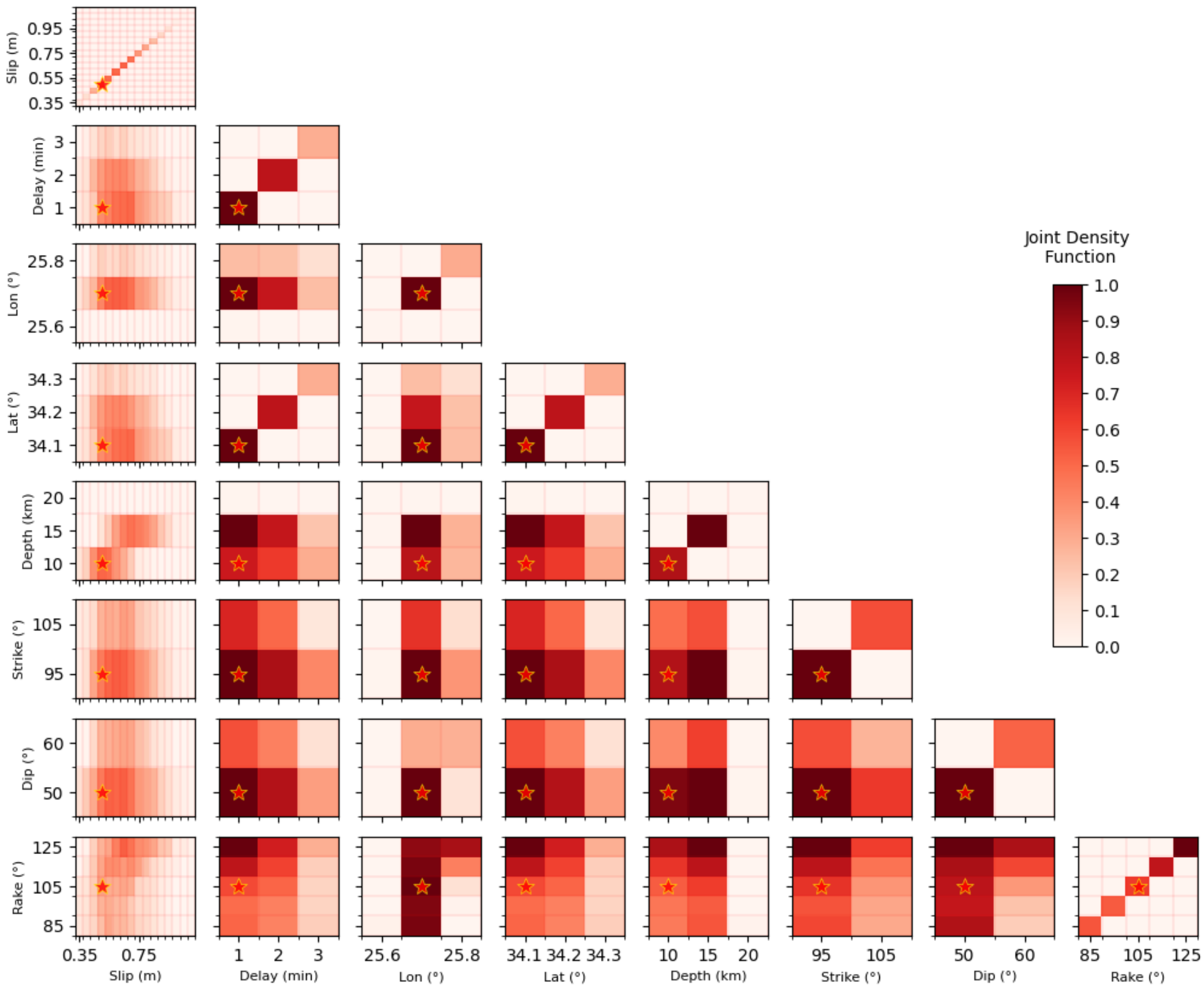

Figure 6: Joint density distribution for each couple of the back-thrust source's parameters, considering the first 5 percent of B plane models, those at the left of the red vertical line in Figure 3a. The red star identifies the best model.

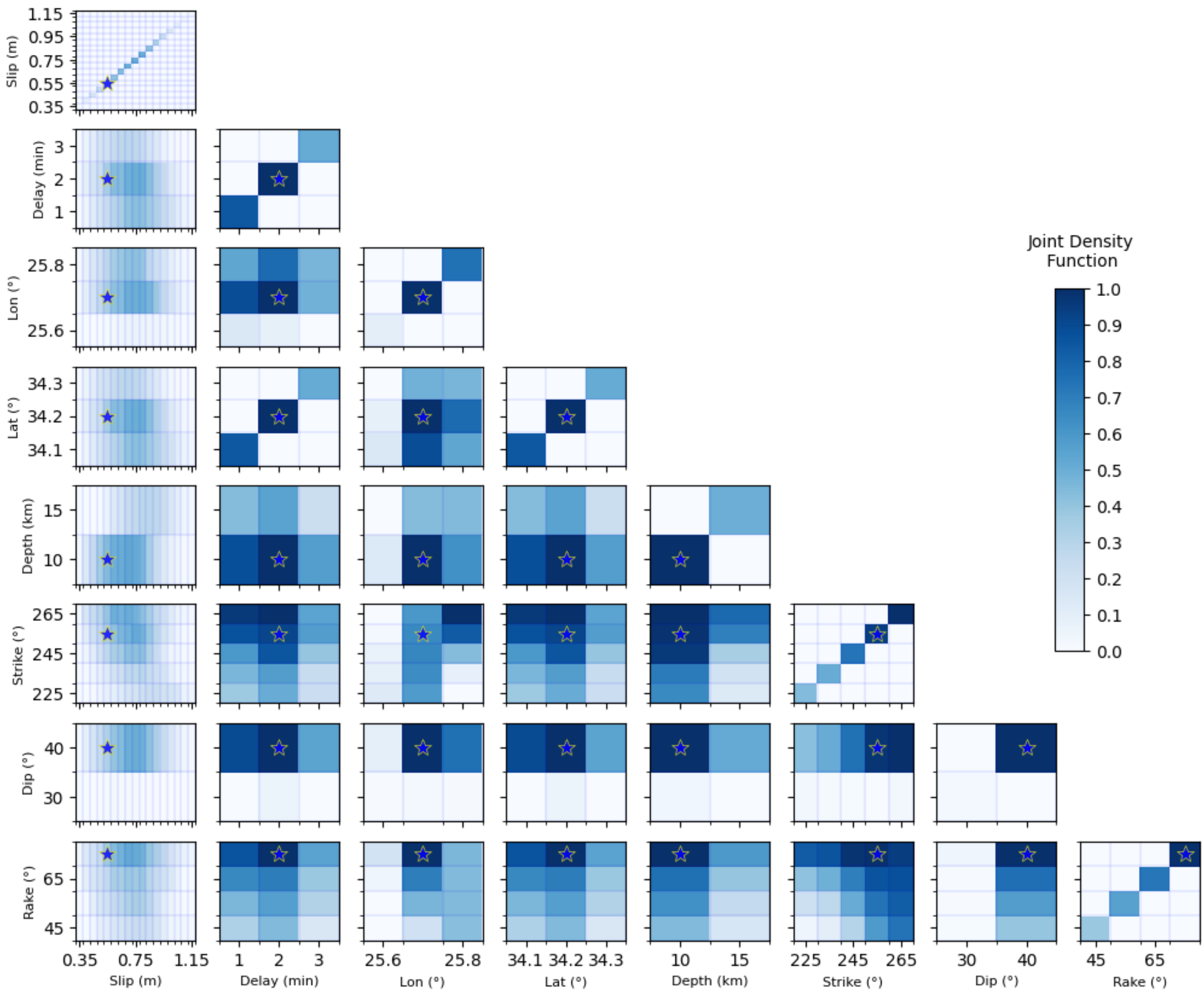

Figure 7: Joint density distribution for each couple of the splay source's parameters, considering the first 5 percent of S plane models, those at the left of the blue vertical line in Figure 3a. The blue star identifies the best model.

The comparison between the observed data and the synthetic ones generated with both the best and the average source models at Ierapetra and Kasos tide gauge is shown in Figure 8; those corresponding to the two planes B (Figure 8a and e) and S (Figure 8c and g) are plotted separately. Both synthetic signals reproduce quite well the first oscillations (covering about 15 minutes). For what concerns the peak at minute 28, the average signals result to be lower.

It is interesting to note a possible "clipping" of the negative peak of the signal at ~ minute 27 caused by the insufficient sampling frequency.

In terms of wave fitting, the comparison between the data and the predictions of the average models is only slightly worse than that found with the best model. Apart from the coseismic slip value, best and average models are similar, especially about the focal mechanism parameters (see Table 2); hence, both the models can be chosen to represent the best sources' ensembles.

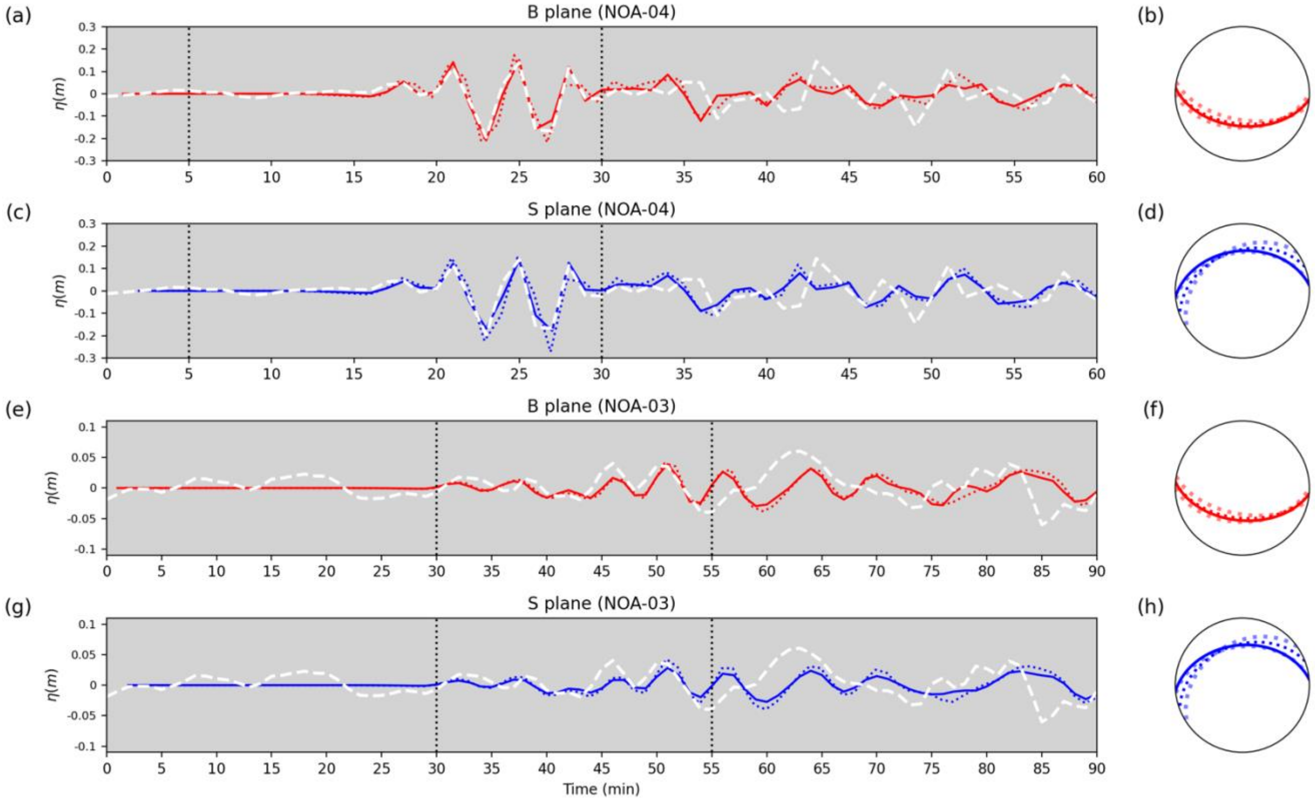

Figure 8: Best (solid lines) and average (dotted lines) marigrams obtained at the two stations. Plots (a) and (c) refer to the Ierapetra tide gauge (NOA-04) while (e) and (g) to the Kasos one (NOA-03). The white dashed line is the observed water elevation at each tide gauge. B plane (in red) refers to the back-thrust solution dipping south; S plane (in blue) refers to the splay fault dipping north. The vertical dotted lines indicate the limits of the time window used for the inversion. On the right of each marigram plot the stereonets (lower hemisphere) show the fault orientations corresponding to the best signal (solid line) and the average one (dotted line) with the variability derived from the standard deviations of Table 2.

The signals belonging to the 5th, 10th, 50th and 100th percentiles of the cost function are shown in Figure 9 to provide a better idea of what a certain cost function implies in terms of waveform fitting with respect to the observed data. Significant discrepancies start to appear when including the models in the 10th percentile and beyond, confirming that all the models with a lower cost function may be equally reasonable solutions.

The synthetic marigrams at Ierapetra reproduce quite well the observed tsunami waveforms for the first cycles of the signal, those carrying most of the source-related information. As discussed above, the agreement worsens as time progresses due to the possibility of not well-modelled propagation complexity around the tide gauge. After roughly half an hour from the tsunami first arrival, there is a larger and larger deviation between the synthetic and the observed marigrams (Figure 8).

Overall, the results do not conclusively indicate that one focal plane should be preferred over another, and both solutions remain possible.

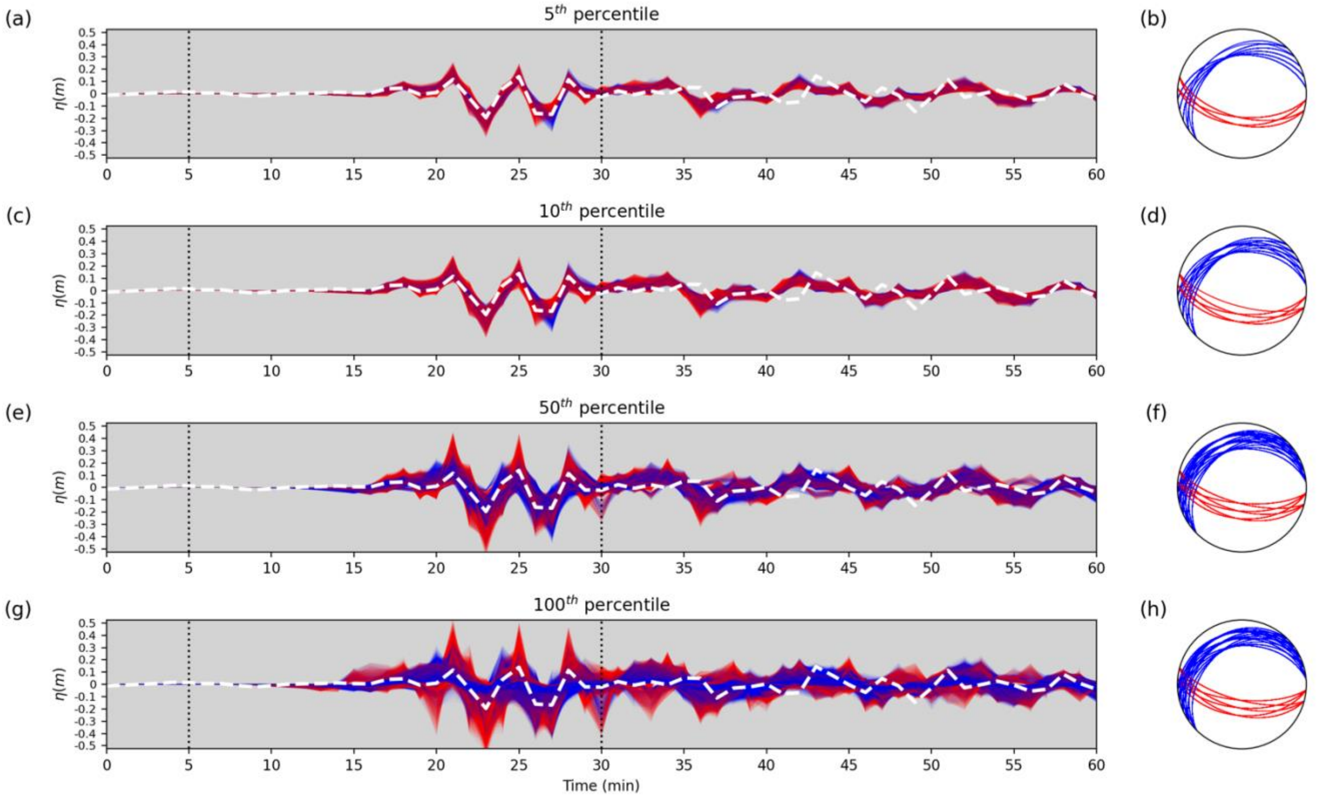

Figure 9 From top to bottom, the left-hand side panels (a, c, e, g) show the marigrams of the events, ordered by cost function value, corresponding to the 5th, 10th, 50th, and 100th percentiles. The white dashed line is the observed water elevation at the Ierapetra tide gauge (NOA-04). The vertical dotted lines indicate the limits of the time window used for the inversion. The stereonets (lower hemisphere) on the

right-hand side (b, d, f, h) show the fault plane variability corresponding to the synthetic waveforms. Red and blue refer to plane B (back-thrust solutions) and plane S (splay fault solutions), respectively, both for waveforms and fault planes.

4 Discussion

We constrained the source model of the 2020 Cretan Passage earthquake (Mw 6.6) by comparing the sea level observations at Ierapetra tide gauge with the synthetic tsunami waveforms.

We could use only one tsunami record (not too distant from the source) in the near field domain to estimate the tsunami source of the 2020 event, whereas we used an additional tide gauge (Kasos) positioned in the far field of the tsunami source as an independent verification of the results. The availability of more instruments would be precious for both real-time operations and event characterisation. Moreover, a better characterisation of harbour response and the implementation in the future of high-resolution in-harbour propagation could be important, particularly considering that deep-sea instruments are nearly absent in the Mediterranean Sea.

We compared the waveforms generated with our solutions with those we simulated using two different source models already published for the 2020 Cretan Passage tsunami: the one presented by Wang et al. (2020; “W” model hereafter), who use the event as a test-case for a hypothetical offshore bottom pressure gauges network around Crete Island, to assist tsunami early warning through real data assimilation, and the Heidarzadeh and Gusman (2021) model (“HG” model hereafter), obtained by inversion of the same tsunami dataset we used in this study.

Figure 10 displays the marigrams calculated with our preferred models together with the waveforms generated by W and HG models. The W waveform tends to overestimate the observed signal, both at Ierapetra and Kasos tide gauge. The HG waveform reproduces well the observed signal at the Ierapetra station, while it overestimates the signal around minute 50 at Kasos. The cost functions associated with the four models, evaluated as described in Section 2, are 0.097, 0.104, 0.583, 0.253 for our B and S planes and for W and HG models, respectively. Using these values, and assuming a rigidity of 33 GPa, consistently with Leonard (2014)’s scaling relationships, the seismic moment associated with the four source models is 6.63, 7.29, 11.9, 11.1 ($\times 10^{18}$) Nm, corresponding to Mw 6.5, 6.6, 6.7, and 6.7, respectively.

The W model, whose waveform presents the largest misfit, consists of a single fault (20 km × 12 km) with a uniform slip of 1.5 m. The epicentre is at 34.205°N, 25.712°E, and the top depth of the fault is 11.5 km; strike, dip, and rake angles are 229°, 31°, and 46°, respectively. These parameters are based on the W-phase focal mechanism solution of the USGS. The slip value is significantly larger than in our preferred models, and it can explain the overestimation. When the same source is used by Wang et al. (2020; see their Figure 9), the agreement between the synthetic and observed waveforms is better. However, Wang et al. (2020) used a bathymetric grid with a resolution of 30 arcsec (~ 925 m), while we used a nested grid approach with a resolution up to 10 m around the tide gauge positions (see Section 2). This likely guarantees a better convergence of the numerical simulation of the relatively short wavelengths characterising this tsunami and explains the difference. When using a lower resolution, the waveforms can only be reproduced by artificially increasing the fault slip. The role of accurate bathymetry is of fundamental importance to ensure accurate tsunami simulations also for source characterisation.

The HG model, with assigned location and focal mechanism (reported in the Introduction), presents a source dimension of 40×30 km and a heterogeneous slip distribution with a maximum slip of 0.64 m and an average slip of 0.28 m. In this case, high-resolution modelling is used around the tide gauges as well. The slip value of our sources is quite larger than their average, but associated with a smaller fault (see Table 1). The overall higher cost function value for the HG model retrieved with our setup can be explained by the fact that the inversion time windows are 13 and 10 minutes for Ierapetra and Kasos tide gauges, respectively, much shorter than the one used in this study (Section 2).

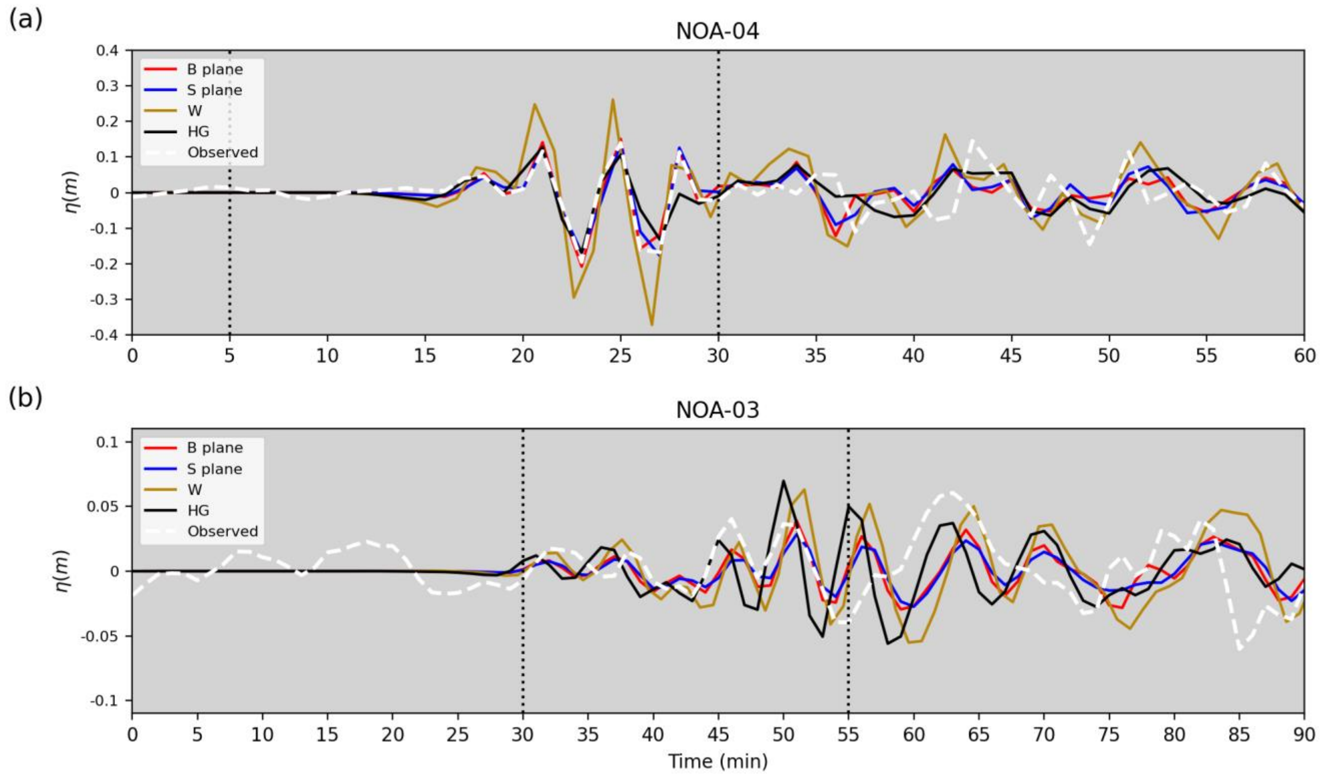

Figure 10: Waveforms obtained at the Ierapetra NOA-04 (a) and Kasos NOA-03 (b) tide gauges by the best source models of the back-thrust solution (the B plane in red), the best of the splay fault solution (the S plane in blue), the fault defined by Wang et al. (2020) and the one by Heidarzadeh and Gusman (2021). The vertical dotted lines indicate the limits of the time window used for the inversion.

Starting from the available focal mechanisms, we explored two thrust faulting solutions (Figure 11), a north-dipping reverse splay fault (plane S) and a south-dipping back-thrust (plane B). We found a slightly better agreement for the waveforms corresponding to the B plane with respect to those of the S plane (Figure 4). However, this difference is not big enough to draw a strong conclusion concerning the causative fault of this earthquake.

Despite this ambiguity between the two fault planes (S and B), still important considerations emerge from this study. Both solutions seem shallow enough to indicate that the earthquake was embedded within the inner parts of the HASZ accretionary wedge, thus excluding either a subduction interface or intraslab earthquake. In particular, the strike of the B plane and the dip of the S plane contribute to excluding a subduction interface earthquake.

From the geological viewpoint, plane B could represent a back-thrust fault accommodating the contraction of the inner parts of the Mediterranean Ridge against the Cretan backstop. This south-eastern Cretan margin is surrounded by the double Pliny and Strabo trenches system, which have been related to back-thrust fault activity (Camerlenghi et al., 1992; Leite and Mascle, 1982; Chaumillon and Mascle, 1997). Back-thrusting is considered to be the cause of the formation of a topographic escarpment separating the wedge from the Inner Ridge backstop (Kopf et al., 2003). The plane S could represent the reactivation of one of the thrusts marking the advancement of the deformation front within the accretionary wedge above the main decollement or a splay fault emanating directly from the subduction interface.

In either case, the orientation of the fault plane and the slip direction are compatible with the long-term kinematic indicators. Within the region of the HASZ where the Cretan Passage earthquake occurred, in fact, the average direction of convergence is ~ 200-220° from GPS velocity data (Reilinger et al., 2006; Floyd et al., 2010; Noquet, 2012) and the azimuth of the maximum horizontal stress (SHmax) is 0-20° (Carafa and Barba, 2013). The splay fault S features a small left-lateral slip component, which is consistent with the increasingly oblique convergence in the eastern branch of the HASZ (Bohnhoff et al., 2005; Yolsal-Çevikbilen and Taymaz, 2012).

The combination of the shallow depth and the high dip angle plays a key role in determining the tsunamigenic potential associated with the fault. The steeper dip angle and the shallower depth tend to produce a vertical deformation whose tsunamigenic potential is more pronounced than that induced by the very low-angle interface earthquakes of similar magnitude. Note, however, that the dip angle of the two proposed solutions is higher than those derived from seismic reflection profiles for these types of thrust faults in the region (Kopf et al., 2003).

For example, the moderate earthquake of Mw = 6.45, which occurred on July 1, 2009 (Bocchini et al., 2020), was the cause of a local tsunami because it ruptured in the overriding crust as for the 2020 Cretan Passage earthquake. Conversely, other larger earthquakes occurred nearby, apparently without generating a tsunami. Just focusing on the portion of the Hellenic trench south of Crete, this is, for example, the case of the Ms 7, December 17, 1952, earthquake occurred at a depth of about 25 km (Papazachos, 1996), and the Ms 6.5, May 4, 1972, earthquake occurred at ~ 40 km depth (Kiratzi and Langston, 1989).

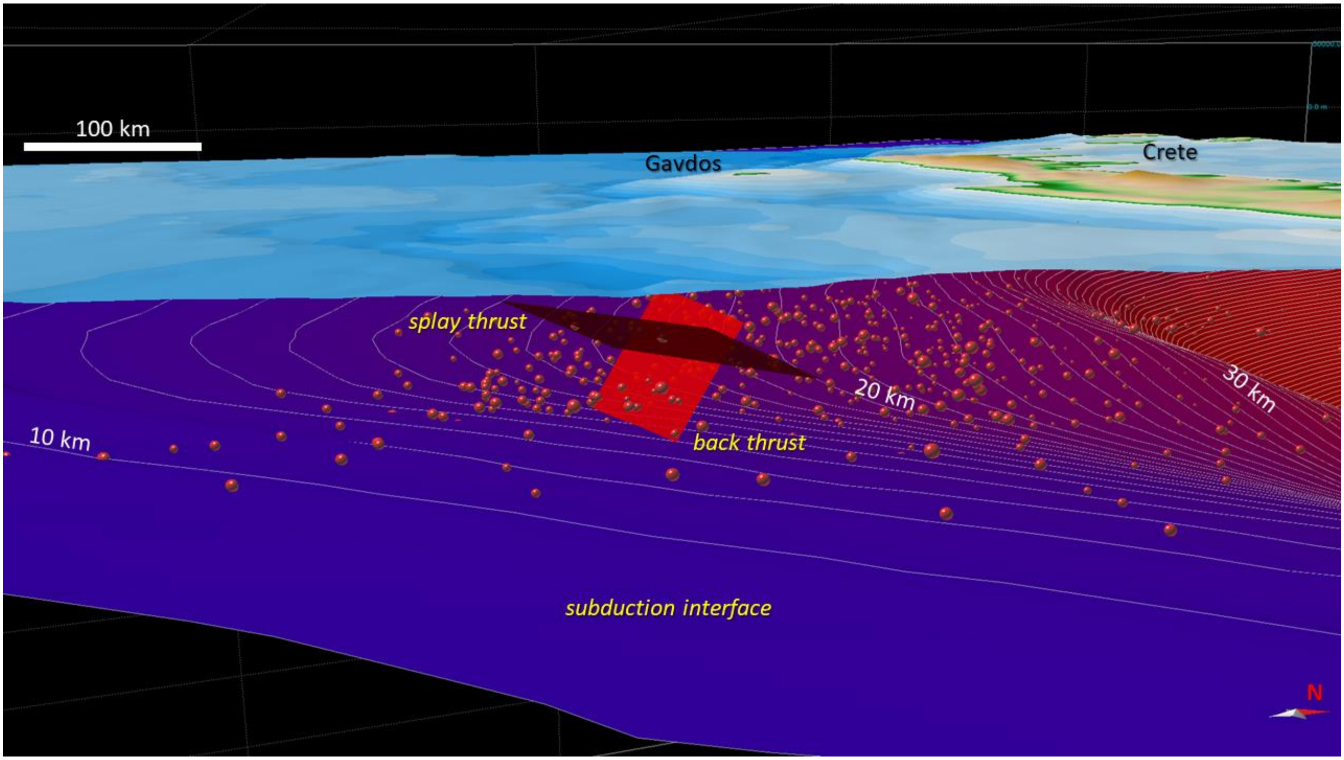

Figure 11: Oblique view, looking westward, of the fault planes obtained in this study and their relation with the subduction interface shown by depth contours (white lines) and the aftershock seismicity (red spheres) until 18/04/2021.

5 Conclusions

We investigated the seismic fault structure and the rupture characteristics of the Mw 6.6, May 2, 2020, Cretan Passage earthquake through tsunami data inverse modelling. Our results confirm the indication from moment tensor solutions that this was a shallow crustal event with a reverse mechanism within the accretionary wedge rather than on the Hellenic Arc subduction interface.

Using just two marigrams, only one of which in the near field with respect to the seismic source, we could highlight important characteristics of this earthquake, especially from a tsunamigenesis perspective, although the adopted method and the limited data available did not prove sufficient to isolate the main focal plane. The sea-level heights recorded at Ierapetra tide gauge identify two possible ruptures: a steeply sloping reverse splay fault and a back-thrust rupture dipping south, with a more prominent dip angle. The a-posteriori appraisal of the ensemble of models tested allows for a slight preference for the south-dipping back-thrust over the splay fault.

Nevertheless, both are high-angle reverse faults in the upper plate above the plate interface with a tsunamigenic potential higher than that of interplate earthquakes of similar or even slightly larger moment magnitude.

This is important for seismic and tsunami hazard assessment, since the presence of shallow crustal ruptures should not be overlooked in an area where subduction interface (interplate) events are also possible. Note that, for example, the recent NEAMTHM18 tsunami hazard model considered the possibility of crustal faults rupturing everywhere in the overriding plate (Basili et al., 2021).

Although the tsunami did not cause damages or victims, the event represents yet another testimony of how such events are frequent and typical in the Mediterranean and, particularly, along the Hellenic arc. In addition to this, the near-source nature of the event should be emphasised. Despite the improvements and developments carried out by the NEAMTWS Tsunami Service Providers in recent years, that have proven to be capable of issuing tsunami messages within 10 minutes after the earthquake origin time (Amato et al., 2021), the early tsunami arrival (tenths of minutes or less) at the closest coasts leaves very little time for warning, which is probably the case in many regions in the world. Then, together with an efficient warning system, education, awareness and preparation remain by far the most cost-effective investments for local tsunamis (Imamura et al., 2019). The 2020 Cretan Passage earthquake is another reminder of the tsunami risk in the Mediterranean Sea, but also of the fact that it is extremely appropriate to promptly react to felt shaking, since also moderate earthquakes that are shallow and occur on steep faults may generate a significant and dangerous tsunami.

Acknowledgements. The research reported in this work was supported by OGS and CINECA under HPC-TRES program award number 2020-01, and co-funded by the Italian flagship project RITMARE. RB acknowledges the resources made available by the SISMOLAB-3D at INGV.

References

Amante, C., and Eakins, B. W. (2009). ETOPO1 1 arc-minute global relief model: procedures, data sources and analysis. NOAA technical memorandum NESDIS NGDC-24. National Geophysical Data Center, NOAA. doi:10.7289/V5C8276M, 2009, last access: 5, 2020.

Amato, A., Avallone, A., Basili, R., Bernardi, F., Brizuela, B., Graziani, L., Herrero, A., Lorenzino, M. C., Lorito, S., Mele, F. M., Michelini, A., Piatanesi, A., Pintore, S., Romano, F., Selva, J., Stramondo, S., Tonini, R., and Volpe, M.: From Seismic Monitoring to Tsunami Warning in the Mediterranean Sea, Seism. Res. Lett., 92, 1796–1816, https://doi.org/10.1785/0220200437, 2021.

Ambraseys, N.: Earthquakes in the Mediterranean and Middle East: A Multidisciplinary Study of Seismicity up to 1900. Cambridge University Press, Cambridge, UK, 947 pp. ISBN 9780521872928. https://doi.org/10.1017/CBO9781139195430, 2009.

Basili, R., Kastelic, V., Demircioglu, M. B., Garcia Moreno, D., Nemser, E. S., Petricca, P., Sboras, S. P., Besana-Ostman, G.

M., Cabral, J., Camelbeeck, T., Caputo, R., Danciu, L., Domaç, H., Fonseca, J. F. de B. D., García-Mayordomo, J., Giardini, D., Glavatovic, B., Gulen, L., Ince, Y., Pavlides, S., Sesetyan, K., Tarabusi, G., Tiberti, M. M., Utkucu, M., Valensise, G., Vanneste, K., Vilanova, S. P., and Wössner, J.: European Database of Seismogenic Faults (EDSF) compiled in the framework of Project SHARE,, https://doi.org/10.6092/INGV.IT-SHARE-EDSF, 2013, last access: May 31, 2021.

Basili, R., Brizuela, B., Herrero, A., Iqbal, S., Lorito, S., Maesano, F. E., Murphy, S., Perfetti, P., Romano, F., Scala, A., Selva, J., Taroni, M., Tiberti, M. M., Thio, H. K., Tonini, R., Volpe, M., Glimsdal, S., Harbitz, C. B., Løvholt, F., Baptista, M. A., Carrilho, F., Matias, L. M., Omira, R., Babeyko, A., Hoechner, A., Gürbüz, M., Pekcan, O., Yalçıner, A., Canals, M., Lastras, G., Agalos, A., Papadopoulos, G., Triantafyllou, I., Benchekroun, S., Agrebi Jaouadi, H., Ben Abdallah, S., Bouallegue, A., Hamdi, H., Oueslati, F., Amato, A., Armigliato, A., Behrens, J., Davies, G., Di Bucci, D., Dolce, M., Geist, E., Gonzalez Vida, J. M., González, M., Macías Sánchez, J., Meletti, C., Ozer Sozdinler, C., Pagani, M., Parsons, T., Polet, J., Power, W., Sørensen, M., and Zaytsev, A.: The Making of the NEAM Tsunami Hazard Model 2018 (NEAMTHM18), Front. Earth Sci., 8, 753, https://doi.org/10.3389/feart.2020.616594, 2021.

Bocchini, G. M., Novikova, T., Papadopoulos, G. A., Agalos, A., Mouzakiotis, E., Karastathis, V., and Voulgaris, N.: Tsunami Potential of Moderate Earthquakes: The July 1, 2009 Earthquake (Mw 6.45) and its Associated Local Tsunami in the Hellenic Arc, Pure Appl. Geophys., 177, 1315–1333, https://doi.org/10.1007/s00024-019-02246-9, 2020.

Bohnhoff, M., Harjes, H.-P., and Meier, T.: Deformation and stress regimes in the Hellenic subduction zone from focal Mechanisms, J. Seismol., 9, 341–366, https://doi.org/10.1007/s10950-005-8720-5, 2005.

Camerlenghi, A., Cita, M. B., Hieke, W., and Ricchiuto, T.: Geological evidence for mud diapirism on the Mediterranean Ridge accretionary complex, Earth and Planetary Sci. Lett., 109, 493–504, https://doi.org/10.1016/0012-821X(92)90109-9, 1992.

Carafa, M. M. C. and Barba, S.: The stress field in Europe: optimal orientations with confidence limits, Geophys. J. Int., 193, 531–548, https://doi.org/10.1093/gji/ggt024, 2013.

Chamot-Rooke, N., Rabaute, A., and Kreemer, C.: Western Mediterranean Ridge mud belt correlates with active shear strain at the prism-backstop geological contact, Geology, 33, 861–864, https://doi.org/10.1130/G21469.1, 2005.

Chaumillon, E. and Mascle, J.: From foreland to forearc domains: New multichannel seismic reflection survey of the Mediterranean ridge accretionary complex (Eastern Mediterranean), Marine Geology, 138, 237–259, https://doi.org/10.1016/S0025-3227(97)00002-9, 1997.

Cirella, A., Romano, F., Avallone, A., Piatanesi, A., Briole, P., Ganas, A., Theodoulidis, N., Chousianitis, K., Volpe, M., Bozionellos, G., Selvaggi, G., and Lorito, S.: The 2018 Mw 6.8 Zakynthos (Ionian Sea, Greece) earthquake: seismic source and local tsunami characterization, Geophys. J. Int., 221, 1043–1054, https://doi.org/10.1093/gji/ggaa053, 2020.

De la Asunción, M., Castro, M. J., Fernández-Nieto, E. D., Mantas, J. M., Acosta, S. O., and González-Vida, J. M.: Efficient GPU implementation of a two waves TVD-WAF method for the two-dimensional one layer shallow water system on structured meshes, Computers & Fluids, 80, 441–452, https://doi.org/10.1016/j.compfluid.2012.01.012, 2013.

Dziewonski, A. M., Chou, T.-A., and Woodhouse, J. H.: Determination of earthquake source parameters from waveform data for studies of global and regional seismicity, J. Geophys. Res.: Solid Earth, 86, 2825–2852, https://doi.org/10.1029/JB086iB04p02825, 1981.

Ebeling, C.W., Okal, E.A., Kalligeris, N. and Synolakis, C.E.: Modern seismological reassessment and tsunami simulation of historical Hellenic Arc earthquakes, Tectonophysics, 530, 225-239, 2012.

Ekström, G., Nettles, M., and Dziewoński, A. M.: The global CMT project 2004–2010: Centroid-moment tensors for 13,017 earthquakes, Physics of the Earth and Planetary Interiors, 200–201, 1–9, https://doi.org/10.1016/j.pepi.2012.04.002, 2012.

EMODnet Bathymetry Consortium, EMODnet Digital Bathymetry (DTM), 2020, available online at: https://doi.org/10.12770/bb6a87dd-e579-4036-abe1-e649cea9881a, 2020, last access March 20, 2021.

Floyd, M. A., Billiris, H., Paradissis, D., Veis, G., Avallone, A., Briole, P., McClusky, S., Nocquet, J.-M., Palamartchouk, K., Parsons, B., and England, P. C.: A new velocity field for Greece: Implications for the kinematics and dynamics of the Aegean, J. Geophys. Res.: Solid Earth, 115, https://doi.org/10.1029/2009JB007040, 2010.

Grünthal, G. and Wahlström, R.: The European-Mediterranean Earthquake Catalogue (EMEC) for the last millennium, J. Seismol., 16, 535–570, https://doi.org/10.1007/s10950-012-9302-y, 2012.

Guidoboni, E., Comastri, A., Traina, G.: Catalogue of Ancient Earthquakes In The Mediterranean Area Up To The 10th Century. SGA, ING, 1994.

Guidoboni, E. and Comastri, A.: The large earthquake of 8 August 1303 in Crete: seismic scenario and tsunami in the Mediterranean area, J. Seismol., 1, 55–72, https://doi.org/10.1023/A:1009737632542, 1997.

Heidarzadeh, M. and Gusman, A. R.: Source modeling and spectral analysis of the Crete tsunami of 2nd May 2020 along the Hellenic Subduction Zone, offshore Greece, Earth, Planets and Space, 73, 1-16, https://doi.org/10.1186/s40623-021-01394-4, 2021.

Kajiura, K.: The leading wave of a tsunami, Bull. Earthquake Res. Inst. Univ., Tokyo, 41, 535–571, 1963..

Kastens, K. A.: Rate of outward growth of the Mediterranean ridge accretionary complex, Tectonophysics, 199, 25–50, https://doi.org/10.1016/0040-1951(91)90117-B, 1991.

Kiratzi, A. A. and Langston, C. A.: Estimation of earthquake source parameters of the May 4, 1972 event of the Hellenic arc by the inversion of waveform data, Physics of the Earth and Planetary Interiors, 57, 225–232, https://doi.org/10.1016/0031-9201(89)90113-1, 1989.

Kopf, A., Mascle, J., and Klaeschen, D.: The Mediterranean Ridge: A mass balance across the fastest growing accretionary complex on Earth, J. Geophys. Res.: Solid Earth, 108, https://doi.org/10.1029/2001JB000473, 2003.

Imamura, F., Boret, S. P., Suppasri, A., and Muhari, A.: Recent occurrences of serious tsunami damage and the future challenges of tsunami disaster risk reduction, Progress in Disaster Science, 1, 100009, https://doi.org/10.1016/j.pdisas.2019.100009, 2019.

Leite, O. and Mascle, J.: Geological structures on the South Cretan continental margin and Hellenic Trench (eastern

Mediterranean), Marine Geology, 49, 199–223, https://doi.org/10.1016/0025-3227(82)90040-8, 1982.

Leonard, M.: Self-Consistent Earthquake Fault-Scaling Relations: Update and Extension to Stable Continental Strike-Slip FaultsSelf-Consistent Earthquake Fault-Scaling Relations, Bull. Seism. Soc. Am., 104, 2953–2965, https://doi.org/10.1785/0120140087, 2014.

Macías, J., Castro, M. J., Ortega, S., Escalante, C., and González-Vida, J. M.: Performance Benchmarking of Tsunami-HySEA Model for NTHMP's Inundation Mapping Activities, Pure Appl. Geophys., 174, 3147–3183, https://doi.org/10.1007/s00024-017-1583-1, 2017.

Mosegaard, K. and Tarantola, A.: Monte Carlo sampling of solutions to inverse problems, J. Geophys. Res.: Solid Earth, 100, 12431–12447, https://doi.org/10.1029/94JB03097, 1995.

NOAA National Geophysical Data Center, ETOPO1 1 arc-minute global relief model. NOAA National Centers for Environmental Information, 2009. available at: https://www.ngdc.noaa.gov/mgg/global/, last Access December 5, 2020.

Nocquet, J.M.: Present-day kinematics of the Mediterranean: A comprehensive overview of GPS results, Tectonophysics, 579, 220–242, https://doi.org/10.1016/j.tecto.2012.03.037, 2012.

Okada, Y.: Internal deformation due to shear and tensile faults in a half-space, Bull. Seism. Soc. Am., 82, 1018–1040, 1992.

Ott, R. F., Wegmann, K. W., Gallen, S. F., Pazzaglia, F. J., Brandon, M. T., Ueda, K., and Fassoulas, C.: Reassessing Eastern Mediterranean Tectonics and Earthquake Hazard From the 365 CE Earthquake, AGU Advances, 2, e2020AV000315, https://doi.org/10.1029/2020AV000315, 2021.

Papadopoulos, G. A., Daskalaki, E., Fokaefs, A., and Giraleas, N.: Tsunami hazards in the Eastern Mediterranean: strong earthquakes and tsunamis in the East Hellenic Arc and Trench system, Nat. Hazards Earth Syst. Sci., 7, 57–64, https://doi.org/10.5194/nhess-7-57-2007, 2007.

Papadopoulos G. A. A Seismic history of Crete: earthquakes and tsunamis, 2000 BC – 2011 AD. Athens: Ocelotos Publications; 2011.

Papadopoulos, G.A., Minoura, K., Imamura, F., Kuran, U., Yalçiner, A., Fokaefs, A., Takahashi, T.: Geological evidence of tsunamis and earthquakes at the eastern Hellenic Arc: correlation with historical seismicity in the Eastern Mediterranean Sea. Research in Geophysics, 2e12, 90-99 (+electr. suppl.), 2012.

Papadopoulos, G. A., Gràcia, E., Urgeles, R., Sallares, V., De Martini, P. M., Pantosti, D., González, M., Yalciner, A. C., Mascle, J., Sakellariou, D., Salamon, A., Tinti, S., Karastathis, V., Fokaefs, A., Camerlenghi, A., Novikova, T., and Papageorgiou, A.: Historical and pre-historical tsunamis in the Mediterranean and its connected seas: Geological signatures, generation mechanisms and coastal impacts, Marine Geology, 354, 81–109, https://doi.org/10.1016/j.margeo.2014.04.014, 2014.

Papadopoulos, G. A., Lekkas, E., Katsetsiadou, K.-N., Rovythakis, E., and Yahav, A.: Tsunami Alert Efficiency in the Eastern Mediterranean Sea: The 2 May 2020 Earthquake (Mw6.6) and Near-Field Tsunami South of Crete (Greece), GeoHazards, 1, 44–60, https://doi.org/10.3390/geohazards1010005, 2020.

Papazachos, B. S.: Large seismic faults in the Hellenic arc, Annali di Geofisica, 39, https://doi.org/10.4401/ag-4023, 1996.

Papazachos, B. and Papazachos, C.: Accelerated Preshock Deformation of Broad Regions in the Aegean Area, Pure appl. geophys., 157, 1663–1681, https://doi.org/10.1007/PL00001055, 2000.

Papazachos, B. C., Karakaisis, G. F., Papazachos, C. B., and Scordilis, E. M.: Earthquake triggering in the North and East Aegean Plate Boundaries due to the Anatolia Westward Motion, Geophys. Res. Lett., 27, 3957–3960, https://doi.org/10.1029/2000GL011425, 2000.

Piatanesi, A. and Lorito, S.: Rupture Process of the 2004 Sumatra–Andaman Earthquake from Tsunami Waveform Inversion, Bull. Seism. Soc. Am., 97, S223–S231, https://doi.org/10.1785/0120050627, 2007.

Polonia, A., Camerlenghi, A., Davey, F., and Storti, F.: Accretion, structural style and syn-contractional sedimentation in the Eastern Mediterranean Sea, Marine Geology, 186, 127–144, https://doi.org/10.1016/S0025-3227(02)00176-7, 2002.

Reilinger, R., McClusky, S., Vernant, P., Lawrence, S., Ergintav, S., Cakmak, R., Ozener, H., Kadirov, F., Guliev, I., Stepanyan, R., Nadariya, M., Hahubia, G., Mahmoud, S., Sakr, K., ArRajehi, A., Paradissis, D., Al-Aydrus, A., Prilepin, M., Guseva, T., Evren, E., Dmitrotsa, A., Filikov, S. V., Gomez, F., Al-Ghazzi, R., and Karam, G.: GPS constraints on continental deformation in the Africa-Arabia-Eurasia continental collision zone and implications for the dynamics of plate interactions, J. Geophys. Res.: Solid Earth, 111, https://doi.org/10.1029/2005JB004051, 2006.

Romano, F., Molinari, I., Lorito, S., and Piatanesi A.: Source of the 6 February 2013 Mw = 8.0 Santa Cruz Islands Tsunami, Nat. Hazards Earth Syst. Sci., 15, 1371–1379, doi:10.5194/nhess-15-1371-2015, 2015.

Romano, F., Piatanesi, A., Lorito, S., Tolomei, C., Atzori, S., and Murphy, S.: Optimal time alignment of tide gauge tsunami waveforms in nonlinear inversions: Application to the 2015 Illapel (Chile) earthquake, Geophys. Res. Lett., 43, 11,226-11,235, https://doi.org/10.1002/2016GL071310, 2016.

Romano, F., Lorito, S., Lay, T., Piatanesi, A., Volpe, M., Murphy, S., and Tonini, R.: Benchmarking the Optimal Time Alignment of Tsunami Waveforms in Nonlinear Joint Inversions for the Mw 8.8 2010 Maule (Chile) Earthquake, Front. Earth Sci., 8, https://doi.org/10.3389/feart.2020.585429, 2020.

Sandanbata, O., Watada, S., Ho, T. C., and Satake, K.: Phase delay of short-period tsunamis in the density-stratified compressible ocean over the elastic Earth, Geophys. J. Int. 226.3, 1975-1985, 2021.

Saltogianni, V., Mouslopoulou, V., Oncken, O., Nicol, A., Gianniou, M., and Mertikas, S.: Elastic Fault Interactions and Earthquake Rupture Along the Southern Hellenic Subduction Plate Interface Zone in Greece, Geophys. Res. Lett., 47, e2019GL086604, https://doi.org/10.1029/2019GL086604, 2020.

Sambridge, M. and Mosegaard, K.: Monte Carlo Methods in Geophysical Inverse Problems, 40, 3-1-3–29, Rev. geophys., https://doi.org/10.1029/2000RG000089, 2002.

Shaw, B., Ambraseys, N. N., England, P. C., Floyd, M. A., Gorman, G. J., Higham, T. F. G., Jackson, J. A., Nocquet, J.-M., Pain, C. C., and Piggott, M. D.: Eastern Mediterranean tectonics and tsunami hazard inferred from the AD 365 earthquake, Nat. Geosci., 1, 268–276, https://doi.org/10.1038/ngeo151, 2008.

Shaw, B. and Jackson, J.: Earthquake mechanisms and active tectonics of the Hellenic subduction zone, Geophys. J. Int., 181, 966–984, https://doi.org/10.1111/j.1365-246X.2010.04551.x, 2010.

Sørensen, M. B., Spada, M., Babeyko, A., Wiemer, S., and Grünthal, G.: Probabilistic tsunami hazard in the Mediterranean Sea, J. Geophys. Res.: Solid Earth, 117, https://doi.org/10.1029/2010JB008169, 2012.

Stiros, S. C.: The AD 365 Crete earthquake and possible seismic clustering during the fourth to sixth centuries AD in the Eastern Mediterranean: a review of historical and archaeological data, J. of Structural Geology, 23, 545–562, https://doi.org/10.1016/S0191-8141(00)00118-8, 2001.

Stucchi, M., Rovida, A., Gomez Capera, A. A., Alexandre, P., Camelbeeck, T., Demircioglu, M. B., Gasperini, P., Kouskouna, V., Musson, R. M. W., Radulian, M., Sesetyan, K., Vilanova, S., Baumont, D., Bungum, H., Fäh, D., Lenhardt, W., Makropoulos, K., Martinez Solares, J. M., Scotti, O., Živčić, M., Albini, P., Batllo, J., Papaioannou, C., Tatevossian, R., Locati, M., Meletti, C., Viganò, D., and Giardini, D.: The SHARE European Earthquake Catalogue (SHEEC) 1000–1899, J. Seismol., 17, 523–544, https://doi.org/10.1007/s10950-012-9335-2, 2013.

Synolakis, C. E., Bernard, E. N., Titov, V. V., Kânoğlu, U., and González, F. I.: Validation and Verification of Tsunami Numerical Models, in: Tsunami Science Four Years after the 2004 Indian Ocean Tsunami: Part I: Modelling and Hazard Assessment, edited by: Cummins, P. R., Satake, K., and Kong, L. S. L., Birkhäuser, Basel, 2197–2228, https://doi.org/10.1007/978-3-0346-0057-6_11, 2009.

Tarantola, A.: Inversion of travel times and seismic waveforms, in: Seismic Tomography: With Applications in Global Seismology and Exploration Geophysics, edited by: Nolet, G., Springer Netherlands, Dordrecht, 135–157, https://doi.org/10.1007/978-94-009-3899-1_6, 1987.

Wang, Y., Heidarzadeh, M., Satake, K., Mulia, I. E., and Yamada, M.: A Tsunami Warning System Based on Offshore Bottom Pressure Gauges and Data Assimilation for Crete Island in the Eastern Mediterranean Basin, J. Geophys. Res.: Solid Earth, 125, e2020JB020293, https://doi.org/10.1029/2020JB020293, 2020.

Woessner, J., Laurentiu, D., Giardini, D., Crowley, H., Cotton, F., Grünthal, G., Valensise, G., Arvidsson, R., Basili, R., Demircioglu, M. B., Hiemer, S., Meletti, C., Musson, R. W., Rovida, A. N. and Sesetyan, K. and Stucchi, M., and The SHARE Consortium : The 2013 European seismic hazard model : key components and results, Bull. of Earthquake Eng., 13, 3553–3596, https://doi.org/10.1007/s10518-015-9795-1, 2015.

Yem, L. M., Camera, L., Mascle, J., and Ribodetti, A.: Seismic stratigraphy and deformational styles of the offshore Cyrenaica (Libya) and bordering Mediterranean Ridge, Geophys. J. Int., 185, 65–77, https://doi.org/10.1111/j.1365-246X.2011.04928.x, 2011.

Yolsal-Çevikbilen, S. and Taymaz, T.: Earthquake source parameters along the Hellenic subduction zone and numerical simulations of historical tsunamis in the Eastern Mediterranean, Tectonophysics, 536–537, 61–100, https://doi.org/10.1016/j.tecto.2012.02.019, 2012.